Extrinsic Fabry-Perot Interferometer for Surface Acoustic Wave Measurement

by

Tuan A. Tran

Thesis submitted to the Faculty of the
Virginia Polytechnic Institute and State University
in partial fulfillment of the requirements for the degree of
Master of Science
in
Electrical Engineering

APPROVED:

Richard O. Claus, Chairman

T. C. Poon

I. Jacobs

May, 1991

Blacksburg, Virginia

Extrinsic Fabry-Perot Interferometer for Surface Acoustic Wave Measurement

by

Tuan A. Tran

Richard O. Claus, Chairman

Electrical Engineering

(Abstract)

A surface acoustic wave sensor based on an extrinsic Fabry-Perot interferometer is described. A single-mode fiber, used as the input/output fiber, and a multimode fiber, used mainly as a reflector, form an air-gap that acts as a low-finesse Fabry-Perot cavity. The Fresnel reference reflection from the glass/air interface at the front of the air-gap interferes with the sensing reflection from the air/glass interface at the far end of the air-gap in the input/output fiber. Strains in the silica tube housing the two fibers change the air-gap length, thereby altering the phase difference between the reference and sensing reflections and modulating the output intensity. A theoretical analysis of the interaction between the strain induced by the acoustic fields and the fiber sensor is presented. Because signal drifting in interferometric sensors is common, a dual optical wavelength stabilization technique is also incorporated into the sensor to minimize the effect. Signal to noise ratios (SNR's) on the order of 39 dB are obtained with a strain sensitivity of 4 $^{o}/\ \mu$strain cm^{-1}.

ACKNOWLEDGEMENTS

I would like to express my sincere appreciation and respect to my Committee Chairman, Professor Richard O. Claus. His guidance, suggestions and supervision have given me the opportunity to fully exploit all my interests in both the engineering and biological sciences. I would also like to thank Professor T. C. Poon and Professor Jacobs for their counsel.

I am also extremely grateful to our research associates Kent Murphy, Mike Gunther and Ashish Vengsarkar for their patient guidance and assistance. Without their help, many of the ideas presented in this thesis would not have been possible. Many thanks to all my colleagues, Chris Koob, Linda Jones and Ann Goette, who made working at FEORC a pleasant and stimulating experience.

Finally, I would like to acknowledge my appreciation to S. E. Baldini at McDonnell Douglas Aircraft for sponsoring this research project.

Table of Contents

List of Illustrations

List of Illustrations

List of Tables

EXTRINSIC FABRY-PEROT INTERFEROMETER FOR SURFACE ACOUSTIC WAVE MEASUREMENT

1.0 INTRODUCTION

Mechanical structures may fail as a consequence of stresses and duration of use. In many cases it is of great importance to determine when the structural integrity over the component's lifetime is compromised. The key is then to develop testing procedures to characterize structural failures in terms of practical measureable parameters. The testing procedures may fall within three broad categories: 1) those of measuring static properties at very low testing speed 2) those of measuring dynamic loading conditions such as high-speed impact, and 3) nondestructive evaluation [1,2]. In both the low and high speed testing procedures, loading of the specimen may cause irreversible damage. Although these procedures are well suited to show the correlation between applied stress and the ensuing damage, a more important goal in a practical system is to develop techniques to anticipate the occurrence of structural failures. Nondestructive evaluation (NDE) offers this alternative. It has become an indispensable tool both as a means to characterize structural damage, and also to forewarn the imminent danger of a catastrophic failure over the lifetime of a component.

Experimentation has shown that prior to a structural failure, microfractures develop [3]. Accompanying these microfractures are ultrasonic acoustic wave pulses which are created by the sudden localized changes in stresses [2]. The

release of the acoustic pulses by materials undergoing microscopic changes of stress state is termed acoustic emission (AE). This natural phenomenon is of considerable interest for applications such as characterizing and locating defects in materials and for anticipating catastrophic failures in structures by monitoring for AE events.

Stress waves associated with acoustic emission have both longitudinal and shear wave components. The generated waves will often travel to the surface and produce a surface deformation field called a Rayleigh surface acoustic wave (SAW) [4]. Many techniques have been employed to detect such surface acoustic waves. The most commonly used standard of comparison for all other measurement devices are piezoelectric transducers (PZT). Piezoelectric devices made of quartz, lithium niobate, lead zirconnate or similar materials are special classes of crystals that generate electric charges when their lattice structures are strained [5]. This unique property is what enables the piezoelectrics to transform surface deformations into electrical signals. In recent years, however, optical fibers have emerged as another important transducer medium. Optical fibers have been implemented into many types of interferometric sensors and used to probe elastic wave fields [7-9]. Increased utilization of fiber optic sensors in NDE is attributed to their many advantages over existing technologies -- avoidance of electromagnetic interference, geometric versatility, higher operating temperature ranges, resistance to many corrosive chemicals, and wide dynamic range.

Most of the fiber optic interferometric sensors (FOIS) rely on one or more of the following strain-optic effects in fibers: 1) the mechanical deformation of the core

diameter due to the Poisson effect, 2) the photo-elastic effect which results in a refractive index change, and 3) the longitudinal deformation of the fiber. These intrinsic effects can either cause a change in the optical propagation constant or in the optical path length of the interferometer, resulting in a phase shift in the sensing arm of the interferometer and observed as a variation of the output intensity [6-11].

In some practical FOIS configurations, in order for the sensor to be sensitive to sub-Angstrom acoustic amplitudes, a long segment of the fiber needs to be exposed to the acoustic field [7]. A long fiber sensing length, however, will often increase the susceptibility of the interferometer to phase modulated noise caused by vibration and temperature variation. Moreover, such conventional interferometers which rely on long sensing segments are more likely to encounter problems of fading and drifting [12]. The work presented here describes a type of optical fiber sensor called an extrinsic Fabry-Perot interferometer (EFPI) that has an external reflecting surface placed close to a single-mode input/output fiber. The proposed sensor has an active sensing length corresponding to an air-gap cavity that measures several micrometers in length, and shows an increase in temperature stability and an improved immunity to phase modulated noise over long gage length designs. Also, an active alignment process used to assemble the sensor guarantees the maximum phase modulation sensitivity required to detect SAW. Fabry-Perot interferometers used in the past to detect ultrasonic waves have suffered from drawbacks such as complicated fabrication procedures, an inability to maintain a quadrature point of operation, susceptibility to extraneous perturbations and demands for long coherence length sources. The EFPI

described in this paper overcomes these drawbacks and is shown to operate in a stabilized manner over long periods of time.

The paper is divided into five chapters. Chapter 2 discusses the theory of surface acoustic waves and the strain mechanisms associated with their propagation. Chapter 3 examines the specifics of the EFPI, presents the interaction of the acoustic wave strain field and the sensor, and creates a model to compare the actual tests with the theory. Chapter 4 finally analyzes some of the results obtained from the EFPI. Chapter 5 summarizes the paper with suggestions for future research.

2.0 THEORY OF SURFACE ACOUSTIC WAVES

2.1 INTRODUCTION

The theory of the propagation of waves in solids was developed during the 19th century but then fell into neglect at the turn of this century. Only recently, within the last twenty years, as a result of new techniques of study and the development of new materials such as plastics and composites, has it become the subject of intense investigation again. The study of propagation often begins with the theory for body or bulk waves. The theory shows that bulk elastic waves can travel in any direction and in any solid, be it isotropic or anisotropic. At any chosen point, these waves can be decomposed into three independent components. One wave component, termed a longitudinal bulk wave is associated with the particle displacement oscillations along the direction of propagation, and is characterized by regions of condensation and regions of rarefraction. The other two components are called transverse waves because the particle motion is perpendicular to the direction of propagation.

Surface acoustic waves (SAW) have also become an object of renewed interest, especially in the areas of composite materials. SAW are also called Rayleigh waves after Lord Rayleigh (John Strutt) who first considered the phenomenon.

Rayleigh developed the theory to elucidate the mechanisms for surface waves traveling on a semi-infinite elastic solid and showed that the particle motion became negligible at a distance of a few wavelengths from the free surface [4]. For nondestructive evaluation, SAW have several important advantages over bulk waves. As a surface phenomenon, they are accessible which help facilitates the task of probing for an AE event; and they also attenuate more slowly than bulk waves. In contrast to bulk waves, the particle motions associated with SAW move in elliptical retrograde paths as the waves travel along the stress-free surface of the solid and may be decomposed into two rather than three orthogonal components. One wave component moves parallel to the free surface whereas the second, normal to the surface [4].

The purpose of this chapter is to provide a theoretical review of SAW based on Newtonian mechanics. The chapter begins by presenting constituent parameters necessary to formulate the theory, followed by the development of the wave equation for an elastic solid. Appropriate boundary conditions are then applied to obtain the particle displacement equation which will be used in Chapter 3 to determine the strains on the optical fiber sensor.

2.2 COMPONENTS OF STRESS AND STRAIN

When a body is subjected to a load or system of loads, two general types of internal forces develop--body forces and surfaces forces [13]. For the purpose of

this discussion, body forces are assumed small in comparison to surface forces and may be neglected. Surface forces are distributed over the surface of the body or across some arbitrary surface within the interior of the body. At any point on the surface, the stress (force per unit area) associated with these forces has components both normal and tangential to the surface. In a Cartesian coordinate system, the stress components can be denoted by σ_{xx}, σ_{xy}, σ_{xz}, σ_{yy} etc., where the first letter in the subscript denotes the direction of stress and the second letter defines the plane of interaction (Fig. 2.1). Within the body, any point P with a fixed rectangular coordinate (x,y,z) can be displaced to a new position (x+Δx, y+Δy, z+Δz). The components of displacement being respectively (u,v,w) can then be given by a Taylor's expansion in the form [14]

$$\mathrm{u} + \frac{\partial \mathrm{u}}{\partial \mathrm{x}}\Delta\mathrm{x} + \frac{\partial \mathrm{u}}{\partial \mathrm{y}}\Delta\mathrm{y} + \frac{\partial \mathrm{u}}{\partial \mathrm{z}}\Delta\mathrm{z} + \ldots ,$$

$$\mathrm{v} + \frac{\partial \mathrm{v}}{\partial \mathrm{x}}\Delta\mathrm{x} + \frac{\partial \mathrm{v}}{\partial \mathrm{y}}\Delta\mathrm{y} + \frac{\partial \mathrm{v}}{\partial \mathrm{z}}\Delta\mathrm{z} + \ldots , \text{ and}$$

$$\mathrm{w} + \frac{\partial \mathrm{w}}{\partial \mathrm{x}}\Delta\mathrm{x} + \frac{\partial \mathrm{w}}{\partial \mathrm{y}}\Delta\mathrm{y} + \frac{\partial \mathrm{w}}{\partial \mathrm{z}}\Delta\mathrm{z} + \ldots . \qquad (2.2.1)$$

From these equations, the following strain quantities can be defined: [4]

$$\epsilon_{xx} = \frac{\partial \mathrm{u}}{\partial \mathrm{x}} , \qquad \epsilon_{yy} = \frac{\partial \mathrm{v}}{\partial \mathrm{y}} , \qquad \epsilon_{zz} = \frac{\partial \mathrm{w}}{\partial \mathrm{z}} ,$$

$$2\epsilon_{yz} = \frac{\partial \mathrm{w}}{\partial \mathrm{y}} + \frac{\partial \mathrm{v}}{\partial \mathrm{z}} , \qquad 2\epsilon_{zx} = \frac{\partial \mathrm{u}}{\partial \mathrm{z}} + \frac{\partial \mathrm{w}}{\partial \mathrm{x}} , \qquad 2\epsilon_{xy} = \frac{\partial \mathrm{v}}{\partial \mathrm{x}} + \frac{\partial \mathrm{u}}{\partial \mathrm{y}} ,$$

$$2\omega_x = \frac{\partial \mathrm{w}}{\partial \mathrm{y}} - \frac{\partial \mathrm{v}}{\partial \mathrm{z}} , \qquad 2\omega_y = \frac{\partial \mathrm{u}}{\partial \mathrm{z}} - \frac{\partial \mathrm{w}}{\partial \mathrm{x}} , \qquad 2\omega_{\mathrm{z}} = \frac{\partial \mathrm{v}}{\partial \mathrm{x}} - \frac{\partial \mathrm{u}}{\partial \mathrm{y}} . \qquad (3.2.2)$$

The first three quantities ϵ_{xx}, ϵ_{yy}, and ϵ_{zz} are the components of infinitesimal strain. These quantities will become important in Chapter 3 when the exact equation for the strains is required to fully develop the acoustic sensor model. The second three components ϵ_{xy}, ϵ_{zx} and ϵ_{xy} are called shear strain. The last three quantities, represented by the symbol ω are called the components of infinitesimal rotation. As shown in Eq. 3.2.2 above, the strains can only be determined if the displacement equations are uniquely specified. The remaining portion of this chapter is devoted to solving for these displacement equations.

If the solid is assumed to be perfectly elastic, the strain and stress are related simply by Hooke's Law which states that each of the six components of stress is at any point a linear function of the six components of strain, viz., [13]

$$\sigma_{ij} = \mathrm{c}_{ijkl}\, \epsilon_{kl} \,, \tag{2.2.3}$$

where

c_{ijkl} = elastic stiffness constants for the medium,

σ_{ij} = stress acting along the i coordinate direction on a surface whose normal is parallel to the j axis and

ϵ_{kl} = shear strain along the k and l coordinate directions.

For a cubic symmetrical crystal, the number of elastic stiffness constants reduces from a field of thirty-six to three [4]. If an isotropic medium is assumed, the values of the coefficients will be independent of the set of axes chosen. Applying

this condition to Hooke's equation, only two independent constants, denoted by λ and μ and known as Lame's constants, will remain. Thus, for a symmetric isotropic medium, the relationship between the stress components and strain components can be written as [4]

$$\begin{aligned}
\sigma_{xx} &= \lambda\Delta + 2\mu\epsilon_{xx} \ , \\
\sigma_{yy} &= \lambda\Delta + 2\mu\epsilon_{yy} \ , \\
\sigma_{zz} &= \lambda\Delta + 2\mu\epsilon_{zz} \ , \\
\sigma_{yz} &= \mu\epsilon_{yz} \ , \\
\sigma_{zx} &= \mu\epsilon_{zx} \ \text{ and} \\
\sigma_{xy} &= \mu\epsilon_{xy} \ ,
\end{aligned} \tag{2.2.4}$$

where

$$\Delta = \epsilon_{xx} + \epsilon_{yy} + \epsilon_{zz} \ ,$$

represents the change in volume of a unit cube and is called dilatation. In addition to the Lame constants, the Young's modulus E, Poisson's ratio ν, and the bulk modulus k can also be used. This enables all the parameters to be derived from just two known constants. A short list of typical constituent parameters for some metals are provided in Table 1.

Table 1 Constituent parameters for some solids [4].

	Steel	*Copper*	*Aluminium*	*Glass*	*Rubber*
Elastic constants (dynes/sq. cm.)					
λ	$11{\cdot}2 \times 10^{11}$	$9{\cdot}5 \times 10^{11}$	$5{\cdot}6 \times 10^{11}$	$2{\cdot}8 \times 10^{11}$	$1{\cdot}0 \times 10^{10}$
μ	$8{\cdot}1$,,	$4{\cdot}5$,,	$2{\cdot}6$,,	$2{\cdot}8$,,	$7{\cdot}0 \times 10^{8}$
E	$21{\cdot}0$,,	$12{\cdot}0$,,	$7{\cdot}0$,,	$7{\cdot}0$,,	$2{\cdot}0 \times 10^{7}$
k	$16{\cdot}7$,,	$12{\cdot}5$,,	$7{\cdot}3$,,	$4{\cdot}7$,,	$1{\cdot}0 \times 10^{10}$
Poisson's ratio ν	0·29	0·34	0·34	0·25	0·5
Density ρ	7·8	8·9	2·7	2·5	0·93
Velocities (metres/sec.)					
c_1	5,940	4,560	6,320	5,800	1,040
c_2	3,220	2,250	3,100	3,350	27
c_e	5,190	3,670	5,090	5,300	46
c_s	2,980	2,120	2,920	3,080	26
c_L	5,420	3,900	5,410	5,460	53

2.3 EQUATIONS OF MOTION FOR SURFACE ACOUSTIC WAVES

The equations of motion in terms of the displacement components (u,v,w) for any point in an elastic medium are derived from Newton's second law of motion, F=ma. Newton's second law in mechanics is analogous to the Helmholtz equation in electromagnetic. Just as the Helmholtz equation is expanded in terms of the electric and magnetic fields to obtain the electromagnetic wave equations, a similar approach can be applied to Newton's equation. Specifically, the Lame constants, the strain, the stress, and other constituent parameters are substituted into Newton's second law to derive the wave equation. Proceeding to obtain the force, the value of stress at the center of each face is multiplied by the area of the face. Shown below is an example of the resultant force at a point P acting in the x-direction and written as a Maclaurin series expansion to the first order [4]

$$\left(\sigma_{xx} + \frac{\partial \sigma_{xx}}{\partial \mathrm{x}}\,\delta\mathrm{x}\right)\delta\mathrm{y}\delta\mathrm{z} \;-\; \sigma_{xx}\delta\mathrm{y}\delta\mathrm{z} + \left(\sigma_{xy} + \frac{\partial \sigma_{xy}}{\partial \mathrm{y}}\,\delta\mathrm{y}\right)\delta\mathrm{x}\delta\mathrm{z} \;-\; \sigma_{xy}\delta\mathrm{x}\delta\mathrm{z} +$$

$$\left(\sigma_{xz} + \frac{\partial \sigma_{xz}}{\partial \mathrm{z}}\,\delta\mathrm{z}\right)\delta\mathrm{x}\delta\mathrm{y} \;-\; \sigma_{xz}\delta\mathrm{x}\delta\mathrm{y}. \qquad (2.3.1)$$

This expression simplifies to

$$\mathrm{F} = \left(\frac{\partial \sigma_{xx}}{\partial \mathrm{x}} + \frac{\partial \sigma_{xy}}{\partial \mathrm{y}} + \frac{\partial \sigma_{xz}}{\partial \mathrm{z}}\right)\delta\mathrm{x}\delta\mathrm{y}\delta\mathrm{z}\ . \qquad (2.3.2)$$

Neglecting body forces such as gravity, the resultant force then equates to

$$\mathrm{ma} = \rho\,(\delta x \delta y \delta z)\,\frac{\partial^2 u}{\partial t^2}\,, \tag{2.3.3}$$

where ρ is the density and the acceleration is written in terms of the displacement quantities. Applying the procedures enumerated above to both the y-direction and z-direction, the following wave equations are obtained [4]

$$\rho\,\frac{\partial^2 u}{\partial t^2} = \frac{\partial \sigma_{xx}}{\partial x} + \frac{\partial \sigma_{xy}}{\partial y} + \frac{\partial \sigma_{xz}}{\partial z}\,,$$

$$\rho\,\frac{\partial^2 v}{\partial t^2} = \frac{\partial \sigma_{yx}}{\partial x} + \frac{\partial \sigma_{yy}}{\partial y} + \frac{\partial \sigma_{yz}}{\partial z} \quad \text{and}$$

$$\rho\,\frac{\partial^2 w}{\partial t^2} = \frac{\partial \sigma_{zx}}{\partial x} + \frac{\partial \sigma_{zy}}{\partial y} + \frac{\partial \sigma_{zz}}{\partial z}\,. \tag{2.3.4}$$

Combining Eq. 2.3.4 with the Lame constants, the three wave equations can be expressed as

$$\rho\,\frac{\partial^2 (u,v,w)}{\partial t^2} = (\lambda + \mu)\left(\frac{\partial \Delta}{\partial x}, \frac{\partial \Delta}{\partial y}, \frac{\partial \Delta}{\partial z}\right) + \mu \nabla^2 (u,v,w)\,, \tag{2.3.5}$$

where $\nabla^2 = \dfrac{\partial^2}{\partial x^2} + \dfrac{\partial^2}{\partial y^2} + \dfrac{\partial^2}{\partial z^2}$ is the Laplace's operator. (2.3.6)

Equation 2.3.5 is the general wave equation for an isotropic elastic solid.

2.4 SOLUTIONS OF THE WAVE EQUATION

The particle displacement components (u,v,w) for SAW are solutions to the general wave equation. The accepted procedures to solving the equation are outlined below:

1. Convert the general wave equation into a suitable coordinate system depending on the geometry of the solid;
2. Obtain the general solutions to the equation using the separation of variables technique;
3. Apply boundary conditions to solve for the constants of the solutions;
4. Obtain the characteristic eigenvalue equation; and
5. Solve the eigenvalue equation to obtain the propagation constant.

For the ease of representation and mathematical treatment, the boundary is taken to be the yz plane with x-axis directed positive toward the interior of the medium. Taking the uniform plane wave to be traveling in the positive z-direction and considering a two-dimensional problem (in the yz plane), the displacements will be independent of y. That is, at a given point (x,z) the displacements will be identical regardless of the y coordinated selected. To further simplify the mathematical procedures, the variables u and w are separated into two potential functions ϕ and ψ such that [13]

$$u = \frac{\partial \phi}{\partial x} - \frac{\partial \psi}{\partial z} \quad \text{and} \tag{2.4.1a}$$

$$w = \frac{\partial \phi}{\partial z} + \frac{\partial \psi}{\partial x} . \qquad (2.4.1b)$$

Using the newly defined potential functions, the dilatation can then be written as

$$\Delta = \epsilon_{xx} + \epsilon_{zz} = \frac{\partial u}{\partial x} + \frac{\partial w}{\partial z} = \nabla^2 \phi , \qquad (2.4.2a)$$

and the rotation as

$$2\omega = \frac{\partial w}{\partial x} - \frac{\partial u}{\partial z} = \nabla^2 \psi . \qquad (2.4.2b)$$

Upon substitution of Eq. 2.4.2 and 2.4.1 into the wave equation Eq. 2.3.5, two intermediary wave equations are formed

$$\rho \frac{\partial}{\partial x}\left(\frac{\partial^2 \phi}{\partial t^2}\right) - \rho \frac{\partial}{\partial z}\left(\frac{\partial^2 \psi}{\partial t^2}\right) = (\lambda + 2\mu) \frac{\partial}{\partial x}\left(\nabla^2 \phi\right) - \mu \frac{\partial}{\partial z}\left(\nabla^2 \psi\right) \qquad (2.4.3)$$

and

$$\rho \frac{\partial}{\partial z}\left(\frac{\partial^2 \phi}{\partial t^2}\right) + \rho \frac{\partial}{\partial x}\left(\frac{\partial^2 \psi}{\partial t^2}\right) = (\lambda + 2\mu) \frac{\partial}{\partial z}\left(\nabla^2 \phi\right) + \mu \frac{\partial}{\partial x}\left(\nabla^2 \psi\right). \qquad (2.4.4)$$

To uncouple the ϕ and ψ dependence from the first equation, differentiating both sides of Eq. 2.4.3 w.r.t. x, both sides of Eq. 2.4.4 w.r.t. to z; and, taking their differences results in [4]

$$\frac{\partial^2 \phi}{\partial t^2} = \frac{\mu + 2\mu}{\rho} \nabla^2 \phi = C_1{}^2 \nabla^2 \phi . \qquad (2.4.5)$$

On the other hand, if both sides of Eq. 2.4.3 is differentiated w.r.t z, and both sides of Eq. 2.4.4 w.r.t x; and taking their differences will result in

$$\frac{\partial^2 \psi}{\partial t^2} = \frac{\mu}{\rho}\nabla^2\psi = C_2{}^2\,\nabla^2\psi\ . \tag{2.4.6}$$

The procedures taken so far have simplified the original elliptical wave equations (Eq. 2.4.3 and 2.4.4) into two second-order differential equations (Eq. 2.4.5 and Eq. 2.4.6). The solutions to a second-order differential equation are well known. Consider as a trial solution to Eq. 2.4.5 and Eq. 2.4.6 a sinusoidal plane wave of frequency $\frac{\omega}{2\pi}$ propagating in the z-direction with phase velocity $c=\frac{\omega}{k}$ and wavelength $\Lambda=\frac{2\pi}{k}$. The solutions to Eq. 2.4.5 and 2.4.6 are [13]

$$\psi(z,t) = A(x)\ e^{j(\omega t\ -\ kz)} \tag{2.4.7}$$

and

$$\phi(z,t) = B(x)\ e^{j(\omega t\ -\ kz)} \tag{2.4.8}$$

where k is the propagation constant, A(x) and B(x) are functions that determine how the amplitudes behave as the waves penetrate a depth x, i.e., the attenuation factor. The next task is then to determine how these amplitude functions vary with depth. If the expression for ϕ is substituted into Eq. 2.4.5, a second-order, linear differential equation with constant coefficients is obtained

$$\frac{d^2B(x)}{dx^2}\ -\ (\ k^2\ -\ h^2)\ B(x) = 0\ , \tag{2.4.9}$$

where

$$h = \frac{\omega}{C_1} . \tag{2.4.10}$$

There are two linearly independent solutions to the expression above. One of the solutions will have an amplitude that becomes divergently large at x=∞ and is discarded. The other is the desired solution

$$B(x) = E\, e^{-qx} , \tag{2.4.11}$$

where

$$q^2 = k^2 - h^2 = k^2 - \frac{\rho\,\omega^2}{\lambda + 2\mu} , \tag{2.4.12}$$

and E is a constant depending on the initial conditions. Similarly, if the procedures are followed for A(x), then

$$\frac{d^2A(x)}{dx^2} - (k^2 - l^2)\, A(x) = 0 , \tag{2.4.13}$$

where $l = \frac{\omega}{c_2}$. (2.4.14)

The relevant solution is

$$A(x) = D\, e^{-sx} \tag{2.4.15}$$

where

$$s^2 = k^2 - l^2 = k^2 - \frac{\rho\,\omega^2}{\mu} . \tag{2.4.16}$$

The potential functions may now be expressed as

$$\psi(z,t) = D\, e^{-sx + j(\omega t - kz)}, \tag{2.4.17a}$$

and

$$\phi(z,t) = E\, e^{-qx + j(\omega t - kz)}\,. \tag{2.4.17b}$$

2.5 EIGENVALUE EQUATION

The solution for the propagation constant k must be determined from the boundary conditions. The boundary conditions require that the tangential stress components σ_{zy} and σ_{xz} and the normal component σ_{xx} vanish at the free surface x=o. Consider the normal stress component σ_{xx} in terms of the ϕ and ψ potentials

$$\sigma_{xx} = \lambda\Delta + 2\mu\,\frac{\partial u}{\partial x} = (\lambda + 2\mu)\,\frac{\partial^2\phi}{\partial x^2} + \lambda\,\frac{\partial^2\phi}{\partial z^2} - 2\mu\,\frac{\partial^2\psi}{\partial x \partial z} = 0\,. \tag{2.5.1}$$

At the surface (x=o), the stress may be expressed as

$$E\left[(\lambda + 2\mu)q^2 - \lambda k^2\right] - 2\,D\mu jsk = 0. \tag{2.5.2}$$

Similarly, for the tangential component of stress σ_{xz}, it is readily shown that

$$\sigma_{xz} = \mu\left(\frac{\partial u}{\partial z} + \frac{\partial w}{\partial x}\right) = \mu\left(2\frac{\partial^2\phi}{\partial x \partial z} - \frac{\partial^2\psi}{\partial x^2} + \frac{\partial^2\psi}{\partial z^2}\right) = 0\ , \tag{2.5.3}$$

and

$$E2jqk + D(s^2 + k^2) = 0. \tag{2.5.4}$$

Equations 2.5.2 and 2.5.4 are two simultaneous equations with two unknown coefficients D and E. Solutions to these equations exist only if the determinant of these coefficients is zero; i.e.,

$$\begin{vmatrix} (\lambda + 2\mu)q^2 - \lambda k^2 & -2\mu sk \\ 2jqk & s^2 + k^2 \end{vmatrix} = 0. \tag{2.5.5}$$

Evaluation of this determinant yields the following eigenvalue equation for k [4]

$$16\left(1 - \frac{h^2}{k^2}\right)\left(1 - \frac{l^2}{k^2}\right) - \left(2 - \frac{\lambda + 2\mu}{\mu}\frac{h^2}{k^2}\right)^2\left(2 - \frac{l^2}{k^2}\right)^2 = 0\ , \tag{2.5.6}$$

which may be simplified to

$$\kappa_1^{\,6} - 8\kappa_1^{\,4} + (\,24 - 16\alpha_1^{\,2}\,)\,\kappa_1^{\,2} + (16\alpha_1^{\,2} - 16) = 0\ , \tag{2.5.7}$$

where

$$\alpha_1{}^2 = \frac{1-2\nu}{2-2\nu} = \frac{\mu}{\lambda + 2\mu}\ , \text{ and} \tag{2.5.8}$$

$$\kappa_1 = \frac{l}{\omega} = \frac{\omega}{kc_2} = \frac{\omega}{k}\sqrt{\frac{\rho}{\mu}}\ . \tag{2.5.9}$$

Equation 2.5.7 is a complicated equation which is generally solved by numerical techniques. Solutions to the equation reveal that only one value of k is allowed for a material with a known Poisson's ratio ν. This characteristic is graphically illustrated in Fig. 2.2 which shows how the propagation constant k varies as a function of all possible Poisson's ratios [14]. For the condition set by Eq. 2.5.7, the particle displacements are expressed as

$$w = \frac{\partial\phi}{\partial z} + \frac{\partial\psi}{\partial x} = -\ (E\ jke^{-qx} + D\ se^{-sx})\ e^{j(\omega t\ -\ kz)}$$

and

$$u = \frac{\partial\phi}{\partial x} - \frac{\partial\psi}{\partial z} = -\ (E\ qe^{-qx} + D\ jke^{-sx})\ e^{j(\omega t\ -\ kz)}\ . \tag{2.5.10}$$

The final expressions for the displacements after eliminating the constant D and taking the real parts are

$$w(z,t) = E\ k\left\{e^{-qx} - \frac{2qs}{(s^2 + k^2)}\ e^{-sx}\right\}\cos(\omega t - kz)\ ,$$

and

$$u(z,t) = E\ q\left\{e^{-qx} - \frac{2f^2}{(s^2 + k^2)}\ e^{-sx}\right\}\sin(\omega t - kz). \tag{2.5.11}$$

The amplitude constant E is dependent on the material properties.

It may be seen from Eq. 2.5.11 that the particle motion for Rayleigh waves is

elliptical retrograde similar to the elliptical direct orbit for surface waves occurring in water. From this equation, the rate of attenuation of the amplitude of the motion in a direction normal to the surface and along the direction of propagation as a function of depth can also be calculated. Figure 2.3 plots the displacement components versus penetration depth generated by Eq. 2.5.11 [13,14,16]. The direction of the elliptical orbit reverses in the interior of the solid and both displacement components decay monotonically. For aluminum at a depth of one wavelength, the amplitude will have decayed to 80% of its value at the surface. Further investigation shows that the attenuation occurs much more rapidly for high frequency acoustic waves. This behaviour is analogous to the "skin effect" encountered in the electromagnetic wave transmission in conductors.

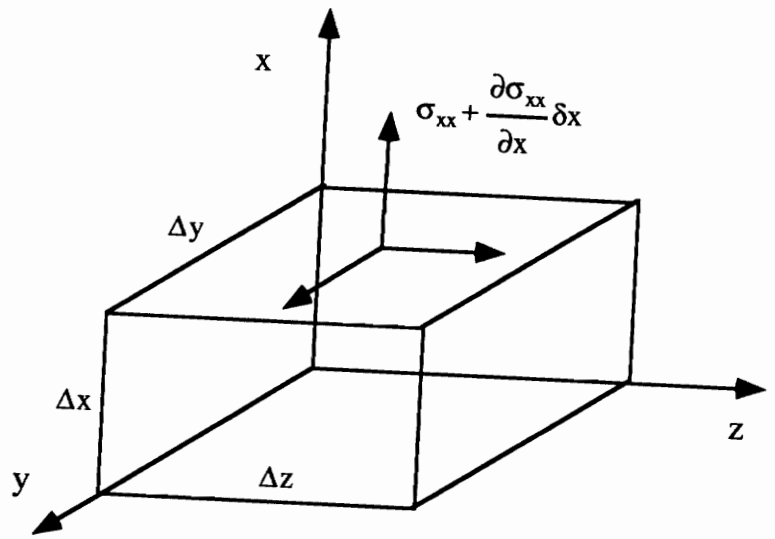

Figure 2.1 Coordinate system and stress components on the faces of a volume element

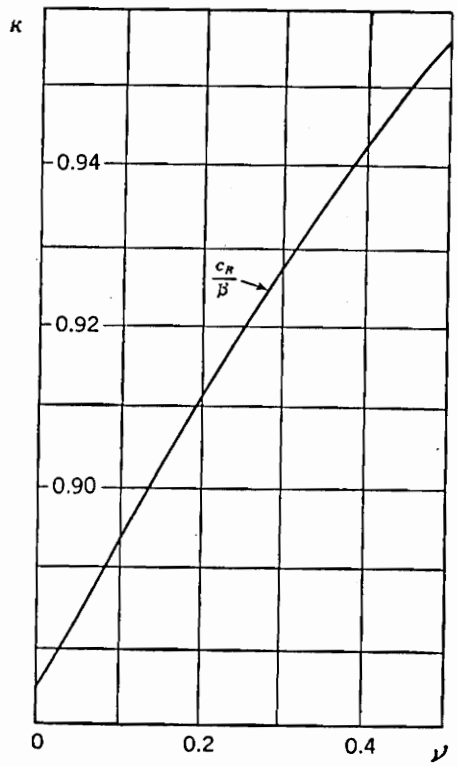

Figure 2.2 Acoustic wave propagation constant as a function of Poisson's ratio [14].

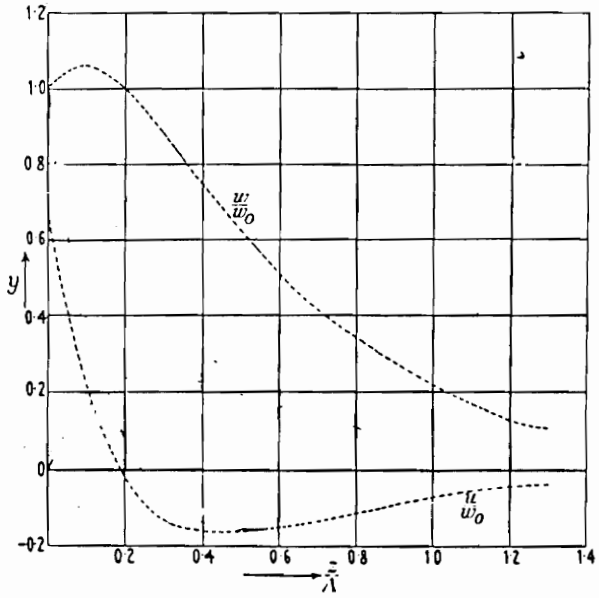

Figure 2.3 Attenuation of SAW's normal and tangential components [14].

3.0 EXTRINSIC FABRY-PEROT INTERFEROMETRIC ACOUSTIC SENSORS

3.1 INTRODUCTION

In the past twenty years, there has been considerable interest in using optical fiber as a sensor for a variety of devices such as hydrophones, magnetometers, strain gauges, as well as vibration and acoustic sensors. One of the configurations which has proven to be very sensitive is the all-fiber interferometer. This sensitivity has enabled the interferometer to measure extremely small phase shifts with resolution in the micro-radian range [6-9].

Interferometers are devices that operate on the principle of interference between two coherent light sources. The principle of optical interference was demonstrated in 1801 by Thomas Young in his classic two slits experiment. When two coherent light sources are combined, regions of bright and dark rings are created. Areas of bright and dark rings correspond to constructive and destructive interference respectively. Young showed that to have constructive interference at any chosen point, the difference in optical path length from the sources to that point must be an even multiple of the wavelength; but to have destructive interference, the path length must be an odd multiple of the half wavelength.

An optical fiber interferometer has two arms which represent Young's coherent light sources. When the optical path length in one of the arms is varied, this results in the modulation of the phase difference between the two arms. By detecting the modulated phase difference at the output of the interferometer, observed as a variation of the intensity, external disturbances can be measured. The EFPI is a phase sensor that uses the difference in optical path length to measure a particular parameter. The interferometer is called extrinsic because the light leaves the fiber to interact with the optical sensor, and the fiber serves only as a optical waveguide to deliver the unmodulated light to the sensor and receive modulated light from it. The distinguishing feature of the EFPI is its narrow sensing region. This allows it to be used as a point sensor. Another feature of the EFPI is that its single optical fiber contains both the reference and sensing legs affording it a great deal of immunity to spurious noises.

The output of the EFPI is directly related to the longitudinal strain produced by the ultrasonic stress waves which cause alternating localized compression and expansion. The derivation of the relationship between the fiber sensor and the strain can be split into four components :

- interrogation of the optical fiber using an extrinsic FPI;
- strain transfer from the elastic solid to the optical fiber sensor;
- strain-optic interaction; and
- detection schemes.

This chapter discusses the acoustic sensor model by relating the components of strain produced by surface acoustic waves to the detected output intensity.

3.2 INTERROGATION OF THE OPTICAL FIBER SENSOR

The setup that is used in the sensor model relies on an air-gap for the sensing region. The EFPI construction was first described by Murphy et. al. [10] and is shown in Fig. 3.1. The EFPI consists of a hollow core fiber capped over the end of a single-mode fiber. A multimode fiber, placed inside the hollow core fiber facing the single-mode fiber, functions as a Fresnel reflector and forms an air-gap that acts as a low-finesse FP cavity. The first reflection at the glass-air interface acts as the reference arm of the interferometer. The second reflection from the surface of the multimode fiber generates the sensing reflection signal. The interference between the two reflections is observed at the output arm of the 2x2 fiber coupler. The interference is caused by axial strains in the hollow core fiber length which displaces the multimode fiber surface reflector and changes the optical path length of the interferometer. Figure 3.2 shows the reflection and transmission of light at the glass-air and air-glass interfaces. Although multiple reflections occur within the cavity, the effect of reflections subsequent to the aforementioned one is negligible because the reflectivities for the air-glass surfaces are less than 4 percent for intensity (see appendix A.3).

In an overview of the mechanics of the sensor, an incident acoustic pressure induces axial strains in the hollow core fiber. At the output arm of the biconical tapered coupler, the intensity of the detected light is modulated as the optical path length is varied. The ratio of the reflected intensity I_r to the incident intensity I_i for the Fabry-Perot interferometer with equal surface reflectivities is expressed as [9]

$$\frac{I_r}{I_i} = \frac{2R(1- \cos\phi)}{1 + R^2 - 2R\cos\phi}, \tag{3.2.1}$$

where

ϕ = round trip phase shift of the laser light inside the cavity; and

R = reflectivity of the fiber surfaces.

The round trip phase shift of the Fabry-Perot can further be expanded into an expression

$$\phi = \frac{4\pi n_0 d}{\lambda_s}, \tag{3.2.2}$$

where

d = air-gap width separation,

n_0 = refractive index of air, and

λ_s = wavelength of the laser.

The narrow air-gap separation between the single-mode and multimode fibers generates the optical path length difference of the interferometer. Noting that the

EFPI used in these sensors have very low finesse, that is R << 1, and assuming the input intensity I_i is unity, the output intensity of Eq 3.2.1 can be approximated by

$$I \propto I_{DC} + I_0 \cos \phi \, . \tag{3.2.3}$$

The equation indicates a sinusoidal relationship between the intensity of the interferometer and the phase difference. The objective now is to recover the phase of the interferometer, and correlate it to the measurand by considering how acoustic signals interact with the fiber.

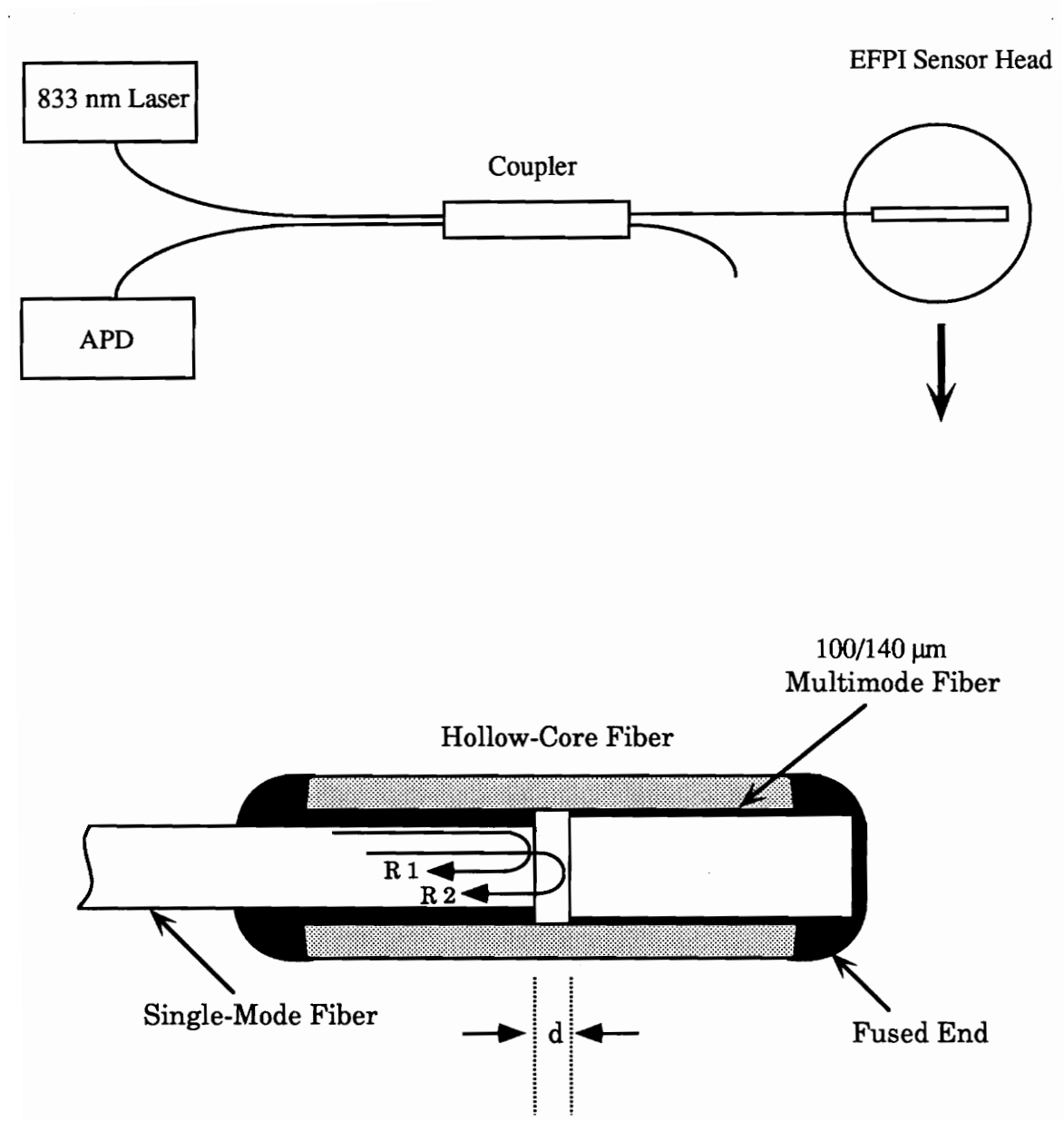

Figure 3.1 Extrinsic Fabry-Perot Interferometer.

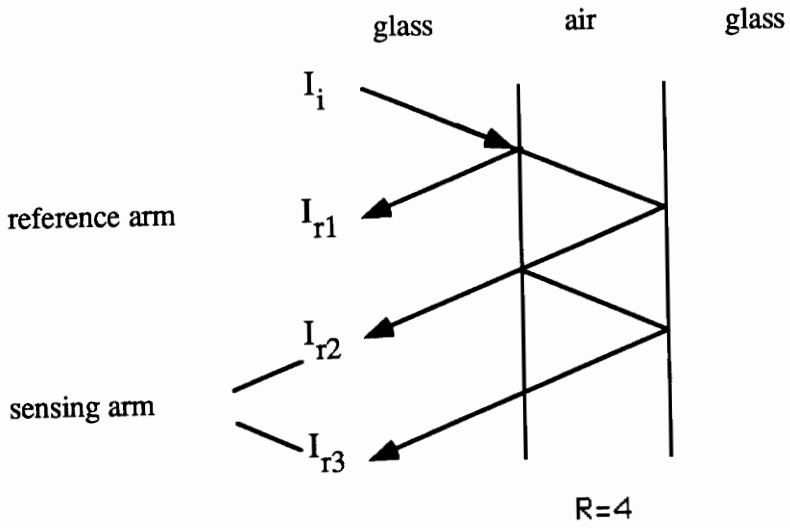

Figure 3.2 Reflection and transmission of light at a planar interface.

3.3 STRAIN TRANSFER BETWEEN THE SENSOR AND THE PERFECTLY ELASTIC SOLID

As surface waves propagate, components of stress are exerted on the supporting elastic solid. These components are imparted to a fiber sensor through the mechanical attachment of the fiber to the surface. The magnitude of the phase change is dependent upon the amplitude of the strain field transferred to the sensor and the configuration in which the fiber is bonded to the test surface. The questions that must be addressed now are how this attachment impacts the fields in the strained body and how the boundary conditions affect the response of the sensor. Ideally, the desired situation is to have the strain field in the solid unaffected by the attached fiber. In the analysis of the sensor, it is assumed that the attached fiber will not significantly alter the strain distribution in the structure. This assumption was experimentally verified by Sirkis [11]. It was shown that in a dark-field isochromatic fringe pattern produced by a photoelastic model of a surface mounted single-mode fiber, the strain field in the specimen is only slightly altered by the presence of the fiber (Fig. 3.3).

The second issue concerns the boundary conditions. The assumption made here is that the strain fields in both the sensor and specimen are continuous; and that the bond between the two is mechanically welded with no slip or gap. This means that the displacement fields in the sensing region and the strained body are equal at the adhesive interface. Having made this assumption, the analysis of the sensor will be greatly simplified because the response of the sensor is mainly caused by

the behavior of the elastic solid. The theory of wave motion in solids has already been discussed. The next step in the analysis is to integrate the body strains with the optical equations of the interferometer.

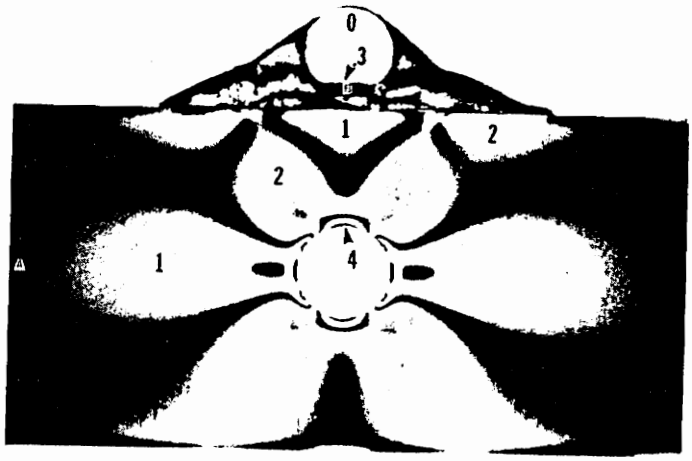

Figure 3.3 Isochromatic pattern [11].

3.4 STRAIN-OPTIC INTERACTION

When an optical fiber is subjected to strains, the optical fiber can experience three possible strain-optic effects:

- mechanical deformation of the radius of the core;
- elongation of the physical gage length of the sensor; and
- via the photo-elastic effect, the modification of the index of refraction.

These effects can either cause a change in the propagation constant or in the optical path length of the interferometer resulting in the optical phase retardation of the signal which propagates in the sensing arm.

For a fiber sensor configuration utilizing intrinsic dielectric mirrors, it was reported by Alcoz, Lee and Taylor that the longitudinal strain of an optical fiber is not a factor because the narrow sensing cavity cannot respond to such high frequency acoustic excitation [9]. Rather, the phase retardation comes mainly from the change in refractive index. However, in the case of an EFPI, the change in the cavity length of the interferometer dominates the phase shift. The theory presented in the next few sections expands on this concept. The analysis assumes the effects of the change in the air refractive index caused by the acoustic pressure and the vibration of the fiber inside the fiber sleeve modulating the phase shift to be minor.

3.5 STRAIN RESPONSE

In order to measure the strain produced by an acoustic signal using the extrinsic FPI, the relationship between the strain in the sensing cavity and the relative phase retardation ϕ must be explicitly established. Let $\epsilon(z)$ be the axial strain in the direction of the sensing cavity axis, where z is the arc length parameter locating the position along this sensing cavity. The total angular phase shift ϕ over the air-gap width d with a constant refractive index is

$$\phi = \int_0^d \left(\frac{d\phi}{dz}\right) dz. \tag{3.5.1}$$

The above expression takes into consideration the case when the strain fields are parallel to the axis of the fiber. In the latter part of the chapter the directional sensitivity of the EFPI will be discussed. An expression for $d\phi/dz$ must now be identified. One approach is to consider the sensing region as being sliced into infinitesimal segments of length Δz as shown in Fig. 3.4 [11]. Since the strain on the sensing region is $(1 + \epsilon_{zz}(z))\Delta z$, the phase retardation is then

$$\Delta\phi = \frac{4\pi n_0}{\lambda_s} \ (1 + \epsilon_{zz}(z))\Delta z \ . \tag{3.5.2}$$

Dividing both sides of Eq. 3.5.2 by Δz and taking the limit as Δz approaches zero, the total phase retardation over a strained sensing region is obtained by integrating Eq. 3.5.1 over the gap separation, viz.,

$$\phi = \frac{4\pi n_0}{\lambda_s} \int_0^d \left[1 + \epsilon_{zz}(z) \right] dz. \tag{3.5.3}$$

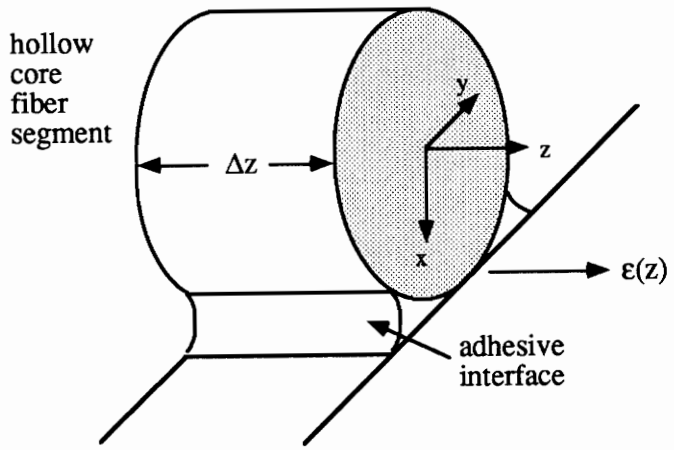

Figure 3.4 Differential fiber segment [11].

3.6 INTEGRATION OF THE SENSOR MODEL WITH THE SURFACE ACOUSTIC WAVE

The next step in developing the analytical model for the acoustic sensor is to interpret the output signals of the EFPI in terms of the particle displacements (u, v, w) associated with ultrasonic stress wave motion in bulk materials. We consider the solid on which the Rayleigh waves are excited as a homogeneous, isotropic, perfectly elastic half space with a plane free boundary. The Rayleigh waves can be stimulated by several methods -- x and y cut quartz plates, comb structures, wedges, $LiNbO_3$ interdigital planar transducer or by the conversion of bulk waves into SAW by an AE event [2,16]. For the ease of presentation, we consider the SAW to have been arbitrarily generated and have propagated into the far field zone. Hence, the near field effect, where each type of transducer has its own set of displacement equations, can be ignored. As a result, the far field SAW can be considered to be plane surface waves so the components of the displacement u and w on the x- and z- axes are independent of the type of transducer used.

With these assumptions, consider a uniform plane wave traveling in the positive z-direction independent of the y-direction, the particle displacement in an isotropic and homogeneous medium was derived in the Chapter 2 and is given here again

$$w(t,x,z) = A\,k\left[e^{-qx} - \frac{2qs}{s^2 + k^2}\, e^{-sx}\right] \sin(\omega_o t - kz)\,. \qquad (3.6.1)$$

The longitudinal strain component created by the stress wave can be derived by differentiating the particle motion with respect to the z direction, i.e.,

$$\epsilon_{zz}(z) = \frac{\partial w}{\partial z} . \tag{3.6.2}$$

Evaluation Eq. 3.6.2 for the strain at the surface (z=0) gives the strain in the axial direction, namely,

$$\epsilon_{zz}(t, 0, z) = - Ak^2 \left[1 - \frac{2qs}{s^2 + k^2} \right] \cos(\omega_o t - kz) . \tag{3.6.3}$$

We now have the strain produced by the stress waves at the surface of a bulk material as a time harmonic quantity. Incorporating Eq. 3.6.3 into 3.5.4 and integrating over the gap separation of the sensor, will then give us

$$\phi(t) = - \frac{8\pi n_0 Ak}{\lambda_s} \left[1 - \frac{2qs}{s^2 + k^2} \right] \sin\left[\frac{kd}{2}\right] \cos\left[\omega_o t - \frac{kd}{2}\right] + \frac{4\pi n_0 d}{\lambda_s} , \tag{3.6.4}$$

the time harmonic phase retardation of the extrinsic Fabry-Perot interferometer. Substituting Eq. 3.6.4 into Eq. 3.2.3 the output intensity of the extrinsic FPI is thus expressed as

$$I(t) = I_{DC} + I_0 \cos\left\{ \alpha A \Gamma \cos\left(\omega t - \frac{kd}{2}\right) + \phi_0 \right\} \tag{3.6.5}$$

where

$$\alpha = -\frac{8\pi n_0 d}{\lambda_s},$$

$$\Gamma = k\left[1 - \frac{2qs}{s^2 + k^2}\right]\sin\left[\frac{kd}{2}\right] \quad \text{and}$$

$$\phi_0 = \frac{4\pi n_0 d}{\lambda_s}.$$

The equation above describes many of the mechanisms that may have an effect on modifying the phase including the static phase ϕ_0 which sets the sensor operating point at quadrature. A more meaningful interpretation of the intensity equation can be realized if it is expanded in terms of the Bessel functions to produce [17]

$$I(t) = I_{DC} + I_0 \left[J_0(\alpha A\Gamma) + 2\sum_{k=1}^{\infty}(-1)^k J_{2k}(\alpha A\Gamma)\cos(2k\omega_0 t + \frac{kd}{2})\right]\cos\phi_0$$

$$- I_o\left[2\sum_{k=0}^{\infty}(-1)^k J_{2k+1}(\alpha A\Gamma)\cos[(2k+1)\omega_0 t + \frac{kd}{2}]\right]\sin\phi_0 . \qquad (3.6.6)$$

For maximum phase modulation sensitivity of an interferometric sensor that has a sinusoidal output pattern, the sensor is set at its quadrature point. When the sensor is operated at quadrature ($\phi_0 = \frac{\pi}{2}$), only odd multiples of ω_0 are present in the output signal. Consequently, only the true frequency of the acoustic signal

and its odd harmonics will be detected; therefore, the photodetector current can be reduced to

$$I(t) = I_{DC} + I_0 [2\ J_1\ (\alpha A\Gamma)\ \cos\omega_0 t\ -\ 2\ J_3\ (\alpha A\Gamma)\ \cos 3\omega_0 t + \ \ldots \qquad (3.6.6)$$
$$+ \text{ higher frequency terms}]\ \sin\phi_o(t)\ .$$

Equation 3.6.6 reveals that i) the detected signal does not have a DC drift, ii) the intensity can be nulled if $\sin\phi_o(t)=0$ (which may occur due to temperature variation), and iii) the third harmonic may be present provided the amplitude A of the acoustic signal is large enough such that the third order Bessel function is significantly above the "effective noise level". For small strains, the argument of the Bessel functions in Eq. 3.6.6 varies over a narrow range. If the argument is less than 0.5, the value of the third order Bessel is approximately zero as seen in Fig. 3.5.

To provide a more complete analysis, the response of the sensor to different frequencies of excitation was also considered; and again utilizing Eq. 3.6.6. A Fortran program (Appendix A.4) was written to simulate and analyze the frequency response of the EFPI. As seen in Fig. 3.6, the output response of the sensor increases monotonically from approximately 1KHz to 1.4 MHz. At frequencies greater than 14 MHz, the output is flat with minor fluctuations occurring at random.

As a final note, the directional sensitivity of the sensor can also be accounted for by multiplying Eq. 3.6.6 by a $\cos\beta$ term, where β is the angle between the axes of the fiber and the strain field. Maximum coupling of strain is experienced when the fiber axis is parallel to the strain. If the sensor is mounted normal to the strain field, then the output is expected to be zero. However, due to the spherical nature of the generated wavefront as opposed to the idealized planar surface wavefront, the component of longitudinal strain may indeed couple to the sensor.

3.7 DETECTION SCHEME

Since the amplitudes of the surface acoustic waves are small, on the order of perhaps 1-100 μm, the strain that is produced on the optical fiber is similarly small. As a result, the detected phase of the sensor will not exceed one fringe. Fringe counting associated with interferometric strain gauges will not be necessary.

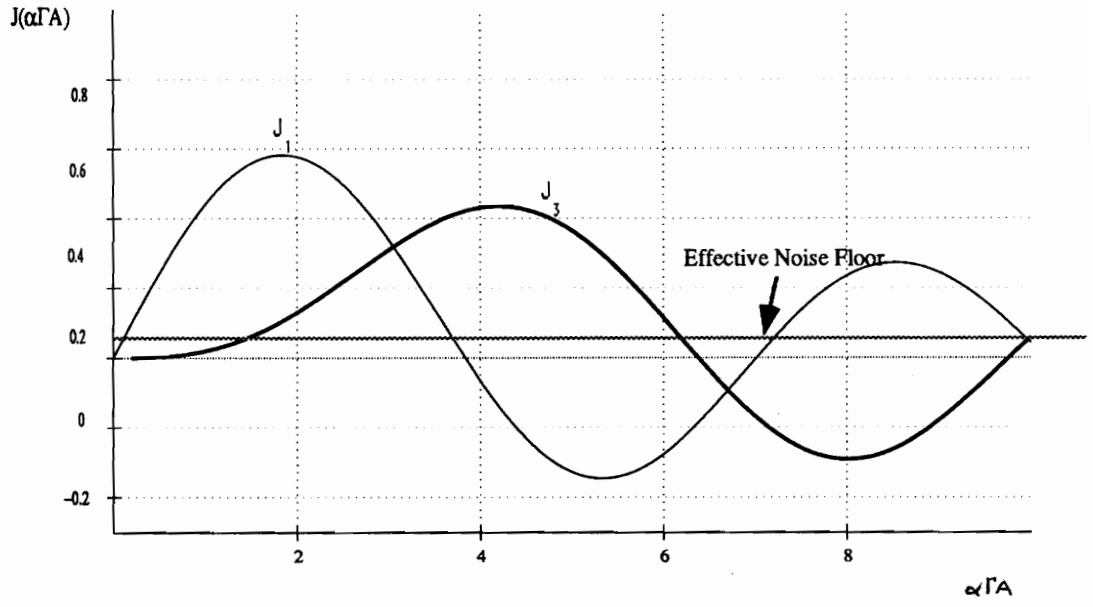

Figure 3.5 First and third order Bessel functions.

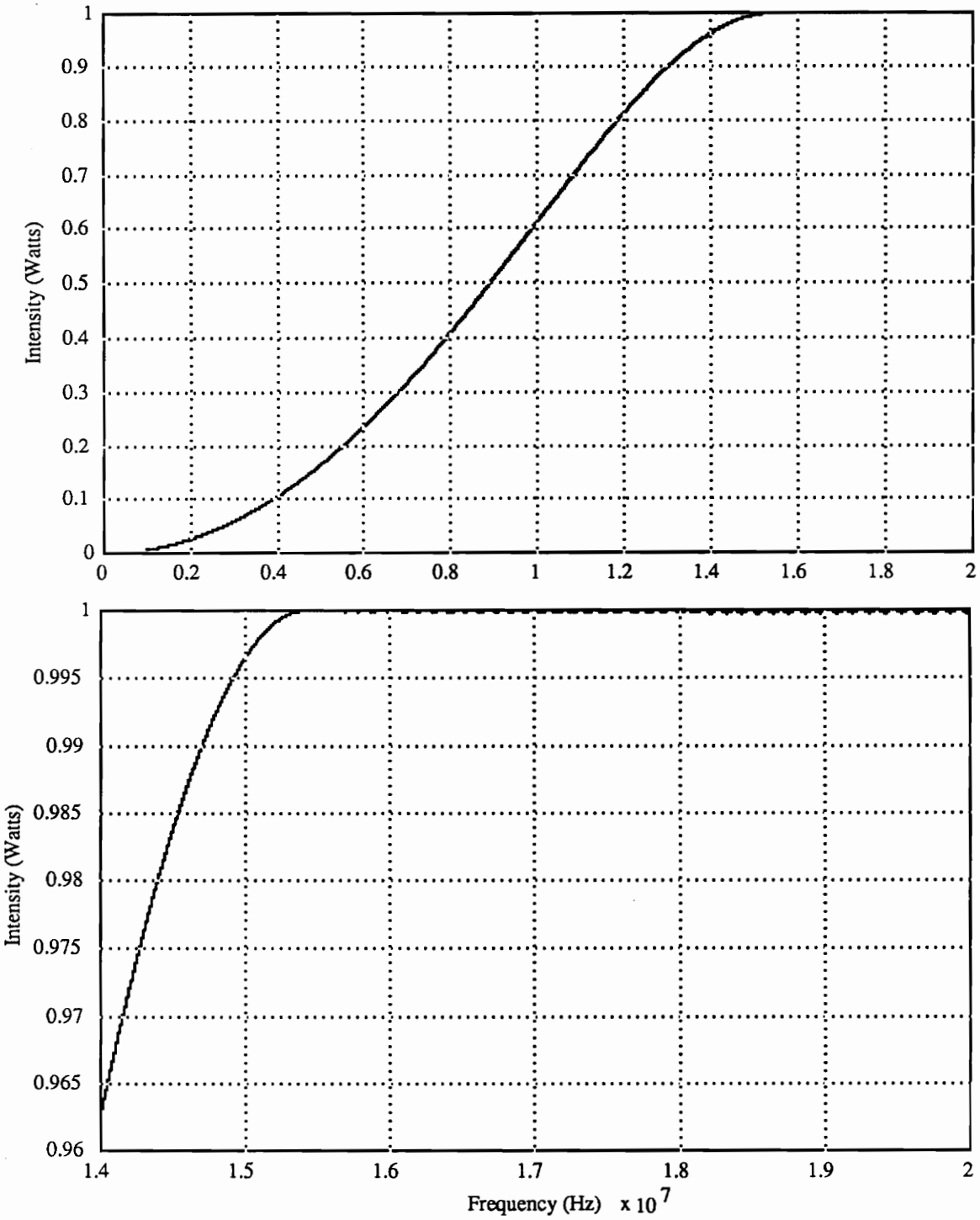

Figure 3.6 Calculated frequency response of EFPI.

a) response plotted for frequency between 0-20 MHz
b) response plotted for frequency between 14-20 Mhz

4.0 EXPERIMENTAL PROCEDURES AND RESULTS

4.1 INTRODUCTION

This chapter describes the characterization of the EFPI SAW sensor under test conditions. Experimental and calculated curves for the sensor are traced, responses of the sensor to frequencies in the range from 1 kHz to 1.9 MHz, direction sensitivity data is obtained and a dual wavelength stabilization technique is demonstrated.

4.2 SENSOR FABRICATION AND DESIGN

The sensor head is assembled by first inserting a cleaved multimode fiber into a hollow core silica fiber. The multimode fiber is then permanently fused to the hollow core fiber. Next, the cap is carefully slipped over the single-mode ($\lambda = 830$ nm) fiber by using a fusion splicer with a three-axes translating stage. To obtain maximum reflections, the flatness of the cleaved multimode fiber surface must be critically monitored. The single-mode fiber is attached to the hollow core fiber

actively by ensuring that the sensor is set at quadrature for maximum sensitivity. The gap separation which sets the quadrature-point is determined interactively by pulsing ultrasonic waves into the translating stage that supports the sensor assembly and monitoring the return lead of the 2 x 2 coupler for signals with the greatest modulation depth. When the maximum sensitivity is achieved, the hollow core fiber is bonded to the single-mode fiber with UV curable epoxy.

In designing the EFPI, consideration was placed on ensuring that the sensor was responding mainly to axial strains rather than transverse vibration of the optical fiber within the walls of the hollow core fiber. This was accomplished by wicking the epoxy all the way to the endfaces of the single-mode and multimode fiber. The change in path length will then arise from either the localized compression or expansion in the air-gap region.

Using the epoxy, the gage length of the sensor can also be set and varied accordingly. The effective gage length of the sensor is determined by the region separated by the epoxy. Thus if the epoxy is applied to the fiber endfaces, then the gage length is the dimension of the air-gap. However, if epoxy is not used and the multimode and single-mode fiber is fused at the ends of the hollow core fiber, the entire alignment tube is the effective gage length.

4.3 OVERALL DESCRIPTION OF SAW SENSOR

The experimental setup for the extrinsic Fabry-Perot interferometric system is shown in Fig. 4.1. Randomly polarized light from a 1 mW laser diode (λ=830 nm) was launched into the input lead of a 3 dB 2x2 fiber coupler. At one output lead of the coupler, the fiber is immersed in index matching gel. At the other output lead, the fiber is spliced onto the EFPI sensing head.

Surface acoustic waves were created by gating a series of 10 μs, 1 MHz ultrasonic wave pulse bursts from a wedge transducer into a test material. The wedge was a Harrisonics piezoelectric transducer mounted on a variable angle plexiglass base. The variable wedge base allows one to generate SAW in different materials by phase matching. The acoustic pulses were generated by gating the Matec amplifier with 1 MHz continuous wave (cw) signals from a Wavetek signal generator.

The avalanche photodiode detector used in the experiment featured high speed and wide bandwidth (DC to 1GHz) response while also offering a high signal to noise ratio (SNR). The wide bandwidth and high speed characteristics are required since the sensor may encounter both low frequency stress waves generated by impacts and high frequency ultrasonic wave pulses generated by AE events.

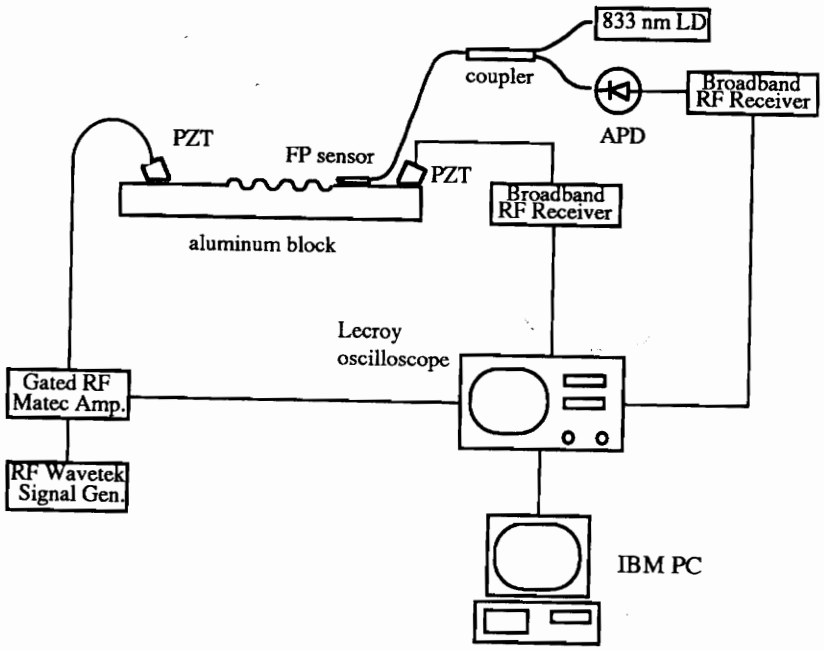

Figure 4.1 Experimental setup for SAW measurements.

4.4 SURFACE STRESS WAVE DETECTION

To detect surface stress waves, the EFPI sensor head was mounted directly on top of a test specimen. An aluminum block of dimensions 5 x 8 x 28 cm served as the test material. To couple acoustic energy from the aluminum block to the sensor head more efficiently, glycerine was applied to the location where the sensor made contact with the aluminum surface. The glycerine provides a mechanical coupling between the silica glass and the aluminum block. To serve as a basis for comparison, a second piezoelectric transducer was placed alongside the Fabry-Perot sensor to detect the same surface stress waves. Figure 4.2 shows the responses of the two sensor types to a 1 MHz cw signal. The top waveform (Fig. 4.2a) is the response of the Fabry-Perot sensor head. Figure 4.2c is the input RF pulse delivered to the wedge transducer. The oscilloscope traces clearly show the interferometer tracking the SAW displacements faithfully, although it has approximately 25% of the sensitivity of the PZT. The SNR of the system was determined to be 39 dB with a sensitivity of $4^0/\mu$strain cm^{-1} for strain measurements.

Low frequency impact stress waves were also detected with the sensor. In another experiment, a pencil lead was broken on top of a 0.6 x 8 x 8 cm aluminum plate, and the sensor's response to the impact was recorded. Fig. 4.3(a) shows the impact point, and an expanded view in shown in Fig. 4.3(b).

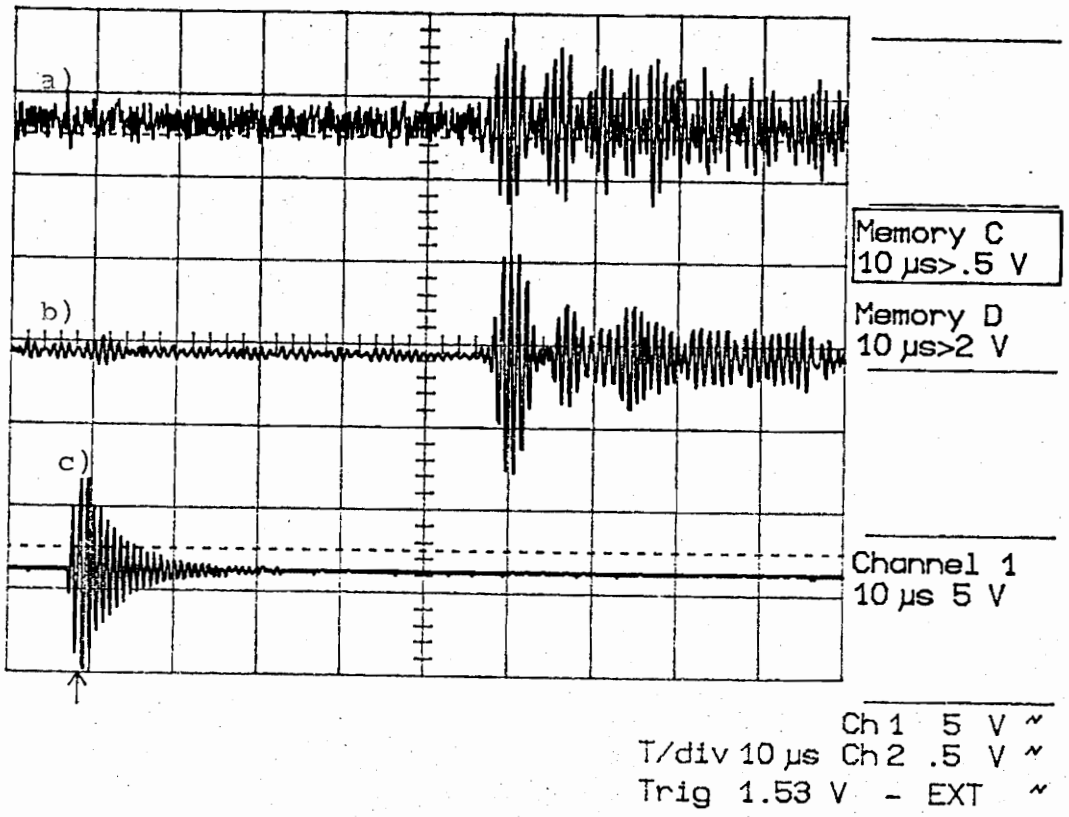

Figure 4.2 Responses of extrinsic FPI and PZT to SAW.

Responses of a) EFPI and b) PZT to an c) RF input pulse.

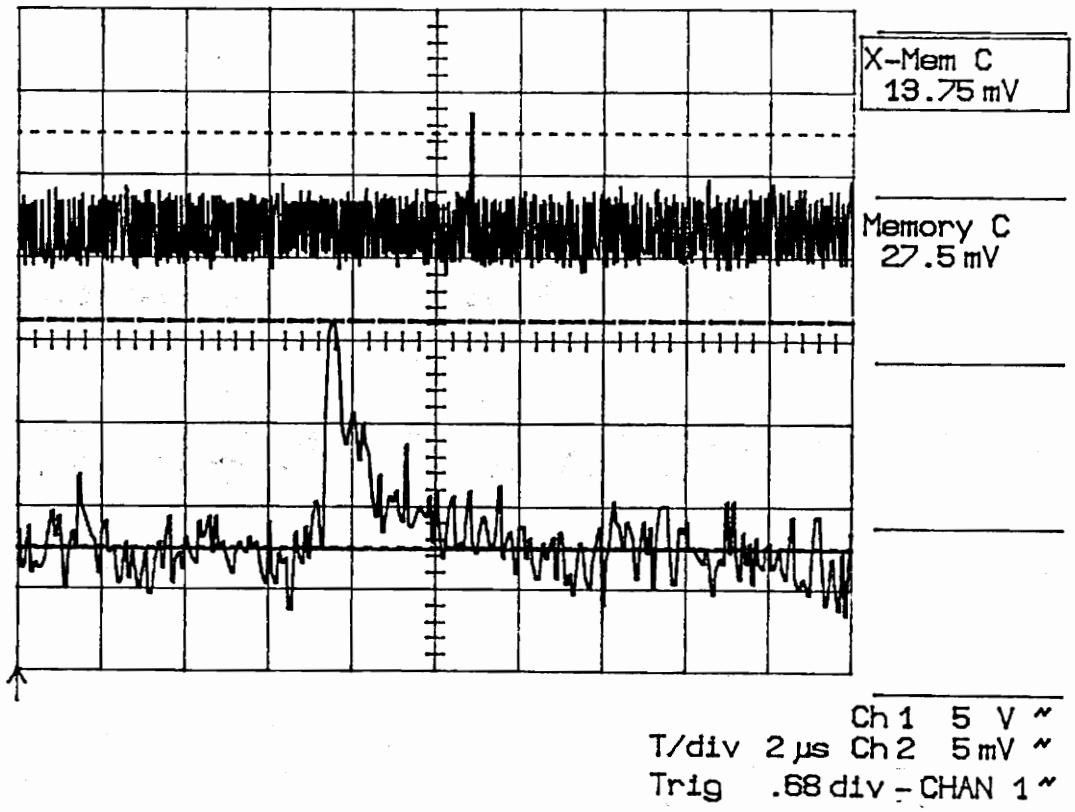

Figure 4.3 Oscilloscope traces of pencil lead break test and the expanded view.

4.5 TRANSFER FUNCTION CURVE

An experiment to test the transfer characteristic of the sensor was also performed. The transfer curve is used to verify the linearity of the sensor's small signal response. When the sensor is maintained at its quadrature point, the output signals of the interferometer are expected to be a linear function of the input signals. The experiment used to test the linearity of the sensor involved a series of procedures of acquiring the waveform using a digitizing storage oscilloscope, transferring and converting the waveform into ASCII formatted data files to an IBM PC, and integrating the Fourier transformed signal using the Matlab program to obtain the spectral power density.

Acoustic pulses ranging from 30% to 90% of the maximum power from the Matec amplifier were launched into an aluminum block to generate surface acoustic waves. The acquired waveforms from the Lecroy digitizing oscilloscope for each of these pulses and their corresponding output signals from the interferometer are transferred into a computer and stored as a binary decimal data file. However, the final format for the post signal processing Matlab program uses ASCII formatted files. Because the data transfer between the PC and Lecroy occurs in binary coded decimal (BCD) format, a BASIC program was written to convert the BCD data files into ASCII format.

Once in computer storage, each of the data files must undergo further processing before output power densities can be determined. Whereas the Lecroy stores a

waveform as 32001 data points, the Matlab program can only acquire a maximum of 8188 data points for each waveform. Therefore, 8k of significant data points were identically extracted from each waveform from a field of 32 K data points. The reduction in data points was achieved by sampling every fourth data point in the conversion process from BCD to ASCII. Although this affected the accuracy of the calculated power density, it was not a significant factor since the same operation was conducted on every data file.

Finally the spectral density of an output signal is calculated by first performing a radix-2 fast Fourier transform (FFT) and then integrating over a frequency range between two amplitude minima. The experimental transfer curve for the EFPI is shown in Fig. 4.4. The graph shows the linear relationship between the incremental output power and the incremental input power. One can also notice that a threshold level of input power is needed to generate the SAW. The FFT of an output waveform shown in Fig. 4.5 shows that the observed 1 MHz output signal was at the same frequency as the input signal and that the third harmonic frequency was not present when the sensor is operated at quadrature ($\phi_0 = \frac{\pi}{2}$). For the condition $\phi_0 = k\pi$, k = 1, 2, ..., the linear response disappeared and the double frequency was observed as predicted by Eq. 3.6.6.

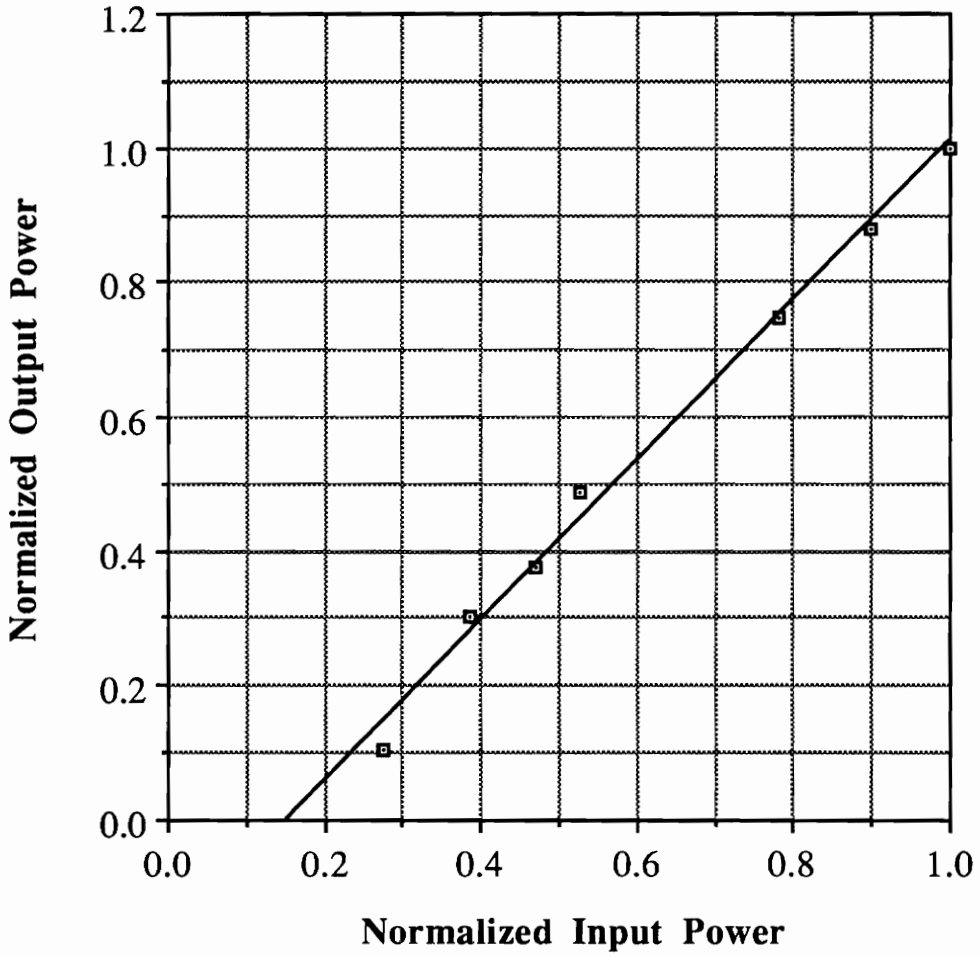

Figure 4.4 Experimental and calculated transfer function curve.

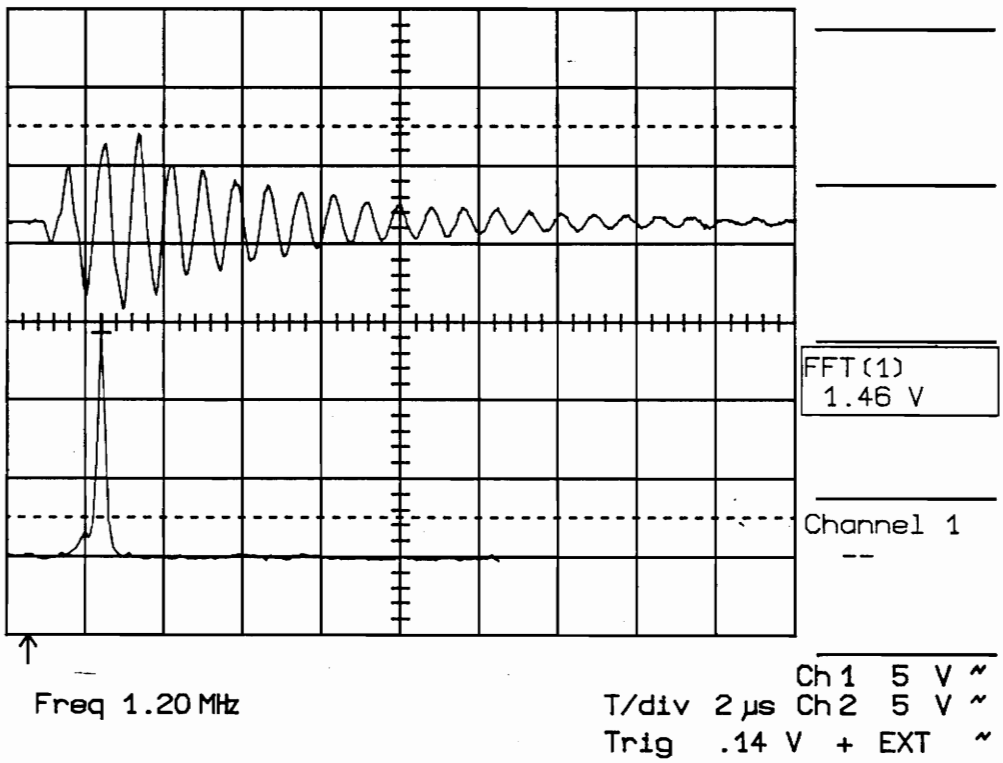

Figure 4.5 FFT of 1.2 MHz input waveform .

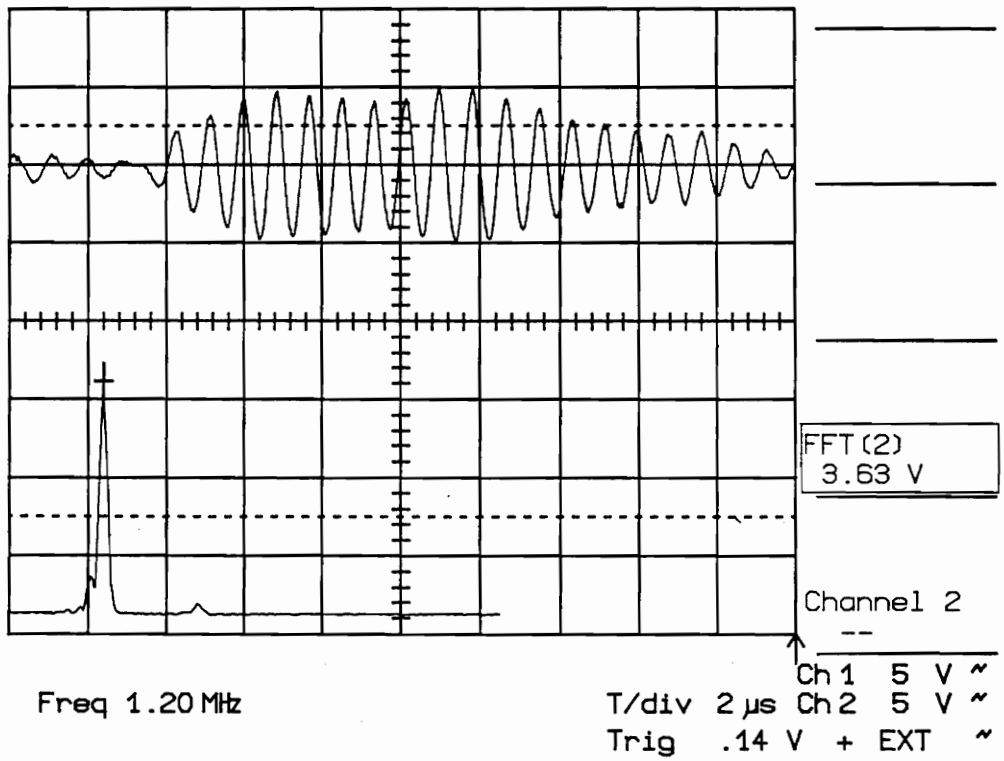

Figure 4.6 FFT of 1.2 MHz detected output waveform.

4.6 FREQUENCY RESPONSE

Another parameter of interest is the frequency response of the sensor. Although the theory was not developed for bulk waves, the experiment characterized the sensor frequency response for longitudinal stress waves. In this test the sensor was embedded in an acrylic resin mold and immersed in a water tank. Using a B&K hydrophone and 2.25 MHz immersion transducer, cw signals were transmitted to the sensor head. The hydrophone had a upper frequency limit of 250 KHz and was tunable from 1-250 KHz, whereas the immersion transducer was tunable over a very narrow range. The setup and the results are diagrammed in Fig. 4.7 and 4.8. Although the frequency response of the sensor can not be directly verified since the output power from the transducer can not be uniformly maintained as the frequency is varied, the EFPI was nevertheless tested for its response from 1 kHz to 150 kHz with the hydrophone and from 1.4 to 1.9 MHz with the transducer. The sensor is expected to be responsive to the intervening frequency from 150 kHz to 1.4 MHz as well. Due to an unnormalized source power, there were pronounced peaks in the detected response of the sensor. The basis for this experiment was mainly to demonstrate the wideband response nature of the EFPI.

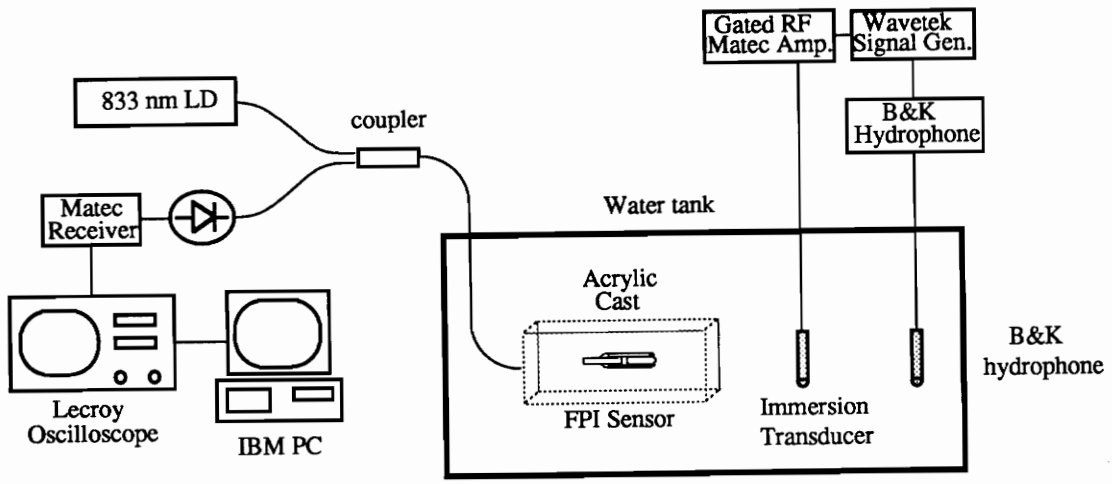

Figure 4.7 Experimental setup used to test the frequency response.

a)

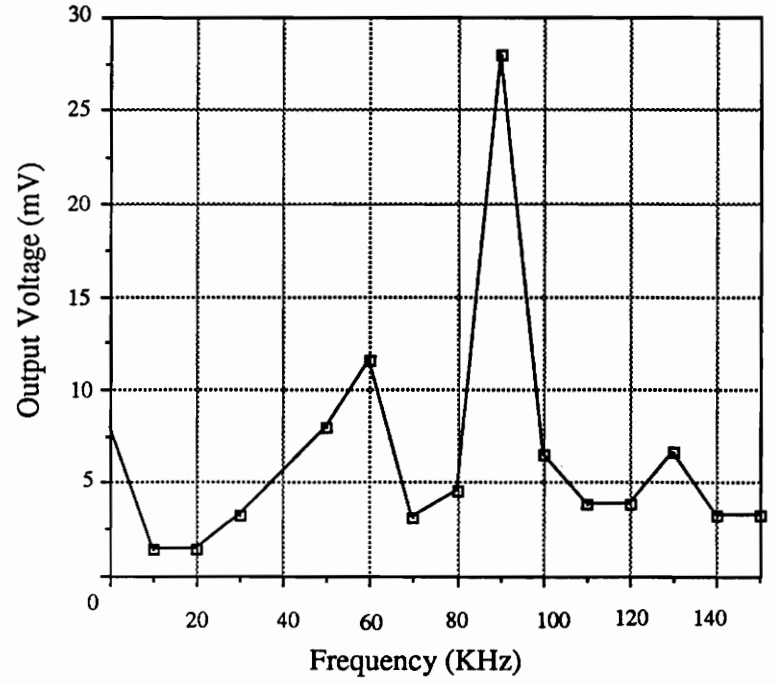

b)

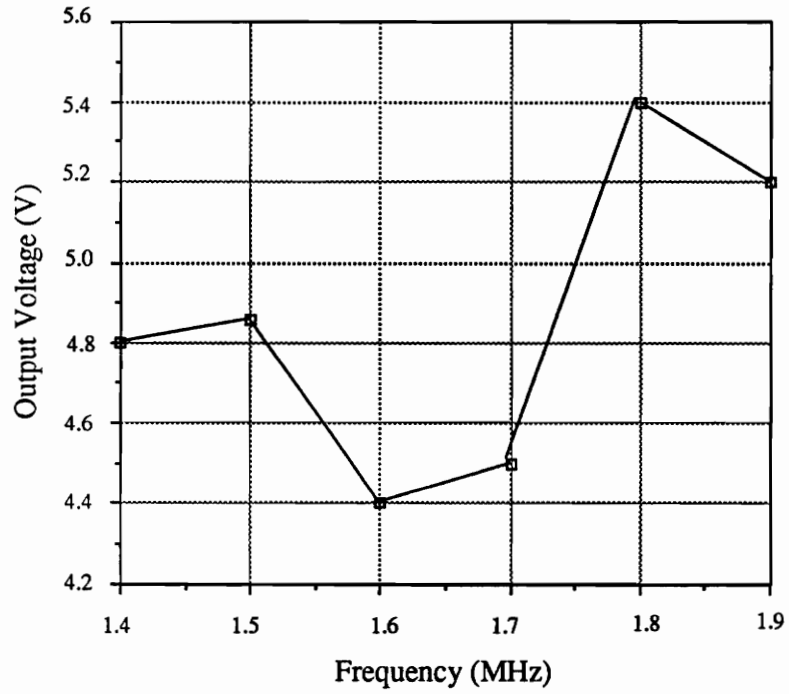

Figure 4.8 Frequency response of EFPI.
a) excitation from hydrophone
b) excitation from Matec amplifier

4.7 DIRECTIONAL RESPONSE

To test the directional response of the EFPI, two sensor designs were implemented. In the first sensor EFPI(1) design, a 2 cm length of hollow core fiber was fastened to the single-mode and multimode fibers at its end as shown in Fig. 4.9(a). The second sensor EFPI(2) had the entire length of the single-mode and multimode fibers epoxied to the hollow core fiber as shown in Fig. 4.9(b). The second sensor design tried to eliminate the effect of vibration of the single-mode fiber within the hollow core fiber. We tested the directional response by rotating both sensors around a 1 MHz wedge transducer mounted on a 40 X 60 X 2 cm aluminum plate. Figure 4.10 displayed the typical response of EFPI(1) as it is being rotated around a SAW source. The detected signal did not decay to zero when the sensor is 90^0 to the source. One may note a rather omnidirectional response. This is in sharp contrast to the EFPI(2) which showed more directional response in the axis of the propagating waves (Fig. 4.11). The responses differ mainly due to the construction of the sensor. In the long gage length sensor, the single-mode and multimode fibers were able to displace laterally inside the hollow core fiber. This resulted in a sensor which displayed a broader sensitivity pattern. In the case of the short gage length EFPI, displacement was limited to the axial direction; thus explaining the reason for the more focused directional response.

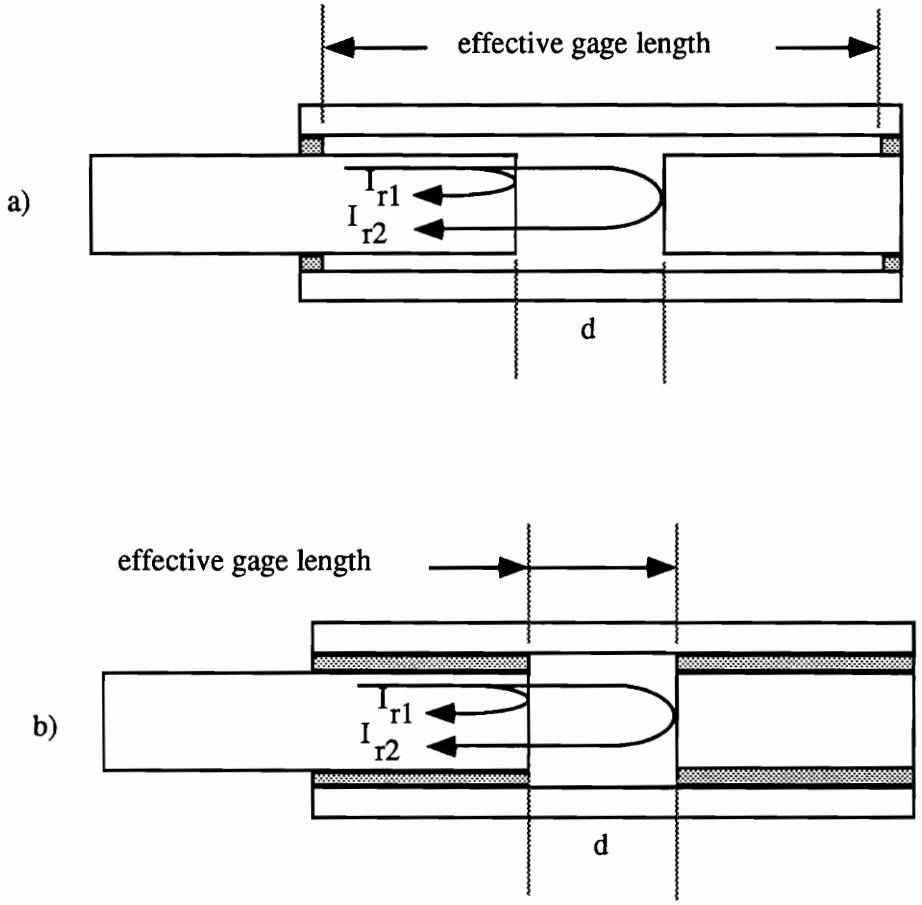

Figure 4.9 EFPI and its effective gage length.

a) large effective gage length design
b) small effective gage length design

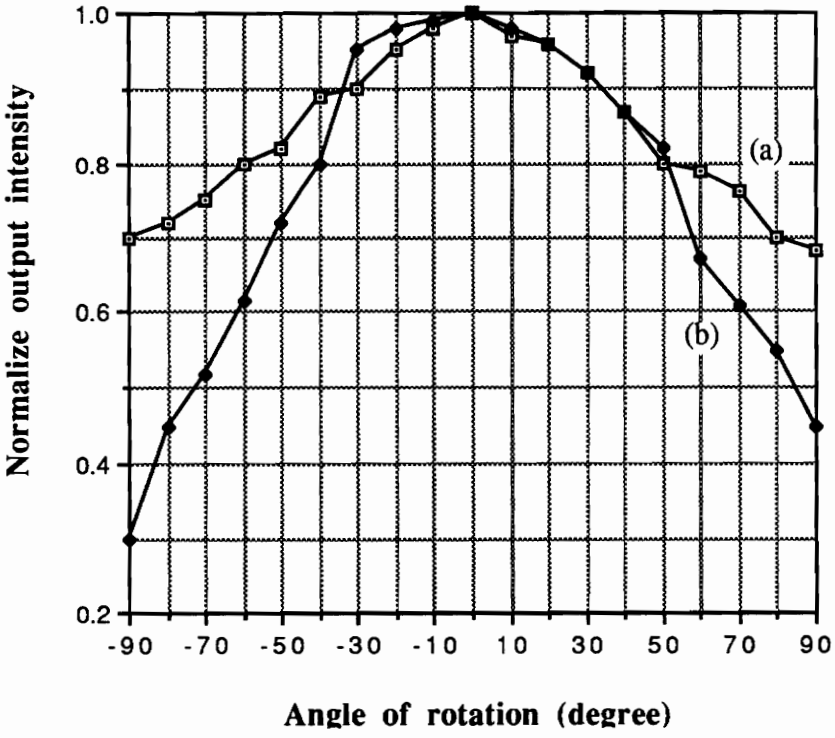

Figure 4.10 Directional response of sensor EFPI.

a) response of sensor EFPI(1) - large gage length
b) response of sensor EFPI(2) - small gage length

4.8 STABILIZED SENSOR OPERATION

In the practical implementation of any interferometric scheme, it is essential to maintain the quadrature point of operation for maximum sensitivity. That is, the phase bias ϕ_o determines the initial point of operation which should lie within the linear range of the sinusoidal output curve. Since signal fading is a common problem in an interferometer, it is advantageous to have two signals out of phase by 90°, so that when one of the signals has a low sensitivity to the phase shift (and hence to the parameter being measured), the other signal has a high sensitivity.

Numerous techniques have been developed to stabilized single-mode interferometric systems. Specifically, the use of frequency and phase modulators to generate heterodyne signals, i.e., active stabilization by tuning the emission frequency of the laser source or phase compensation using piezoelectric devices to modulate the reference fiber, have been used [12,18]. These seemingly effective stabilization techniques are, however, impractical when applied specifically to the EFPI. A tunable laser is prohibitively costly for a practical sensor system and access to the reference arm to actively phase compensate the sensor is hampered because the single-mode fiber contains both arms of the interferometer. The sensor can still be stabilized by an alternate demodulation scheme because of the unique structure of the EFPI. The proposed method uses a two wavelength scheme as shown in Fig. 4.11.

The technique used to generate two phase shifted signals utilizes two laser sources,

one at λ_1 = 780 nm and the second at λ_2 = 830 nm. In the figure, both laser sources launch light into the opposing ends of the air-gap cavity via the two 2 x 2 couplers. Since both sources encounter the same gap separation, the individual optical path lengths ϕ_1 and ϕ_2 are solely dependent on their wavelengths. The proper spacing to create a 90° phase shift is obtained through active alignment. In Fig. 4.12(a) we plot the output curves for the sensor operated at the individual 780 and 830 nm wavelengths. Notice that at points A and C both waveforms are in phase. In the context of the operation of the sensor working at both wavelengths, if the gap separation is set at the spacing specified by points A and C (d = 0 and d = 12.6 μm, respectively), then the sensor at both wavelengths would be out of quadrature simultaneously. Similarly, at point B (d = 6.3 μm) where the waveforms are 180^0 out of phase, both wavelengths are out of quadrature. Hence, we would want to avoid spacing the air-gap at dimensions specified by points A, B, and C.

Contrasting the situation shown in Fig. 4.12(a) with what is shown in Fig. 4.12(b), a 90^0 phase shift is observed between the curves indicated by points Q1 and Q2 where the gap displacement is 3.15 μm. The 830 nm wavelength at point Q1 would be insensitive to acoustic signals. However, with the same gap spacing indicated by point Q2, where the 780 nm wavelength laser is being biased at quadrature, the sensor would be sensitive to an acoustic field. The experimental results given in Fig. 4.13(a) and 4.13(b) demonstrated the capability for the continuous tracking of a measurand using the dual wavelength stabilization scheme. As the sensor is heated, the EFPI cycles in and out of its quadradure point for both wavelengths, but as shown in the figures the signal fading does not

occur simultaneously. With the dual-wavelength setup, the acoustic signal is either tracked by the 780 nm or 830 nm laser. Calibrating the sensor at both wavelengths allows stabilized and continuous operation despite temperature and other externally induced drifts.

We emphasize the improved stability provided by two sources. Whereas the sensor implemented using an individual wavelength loses sensitivity at every multiple of 390 nm or 416 nm respectively, the present setup spaces these positions to 6.3 μm. The range of sensitivity could theoretically be expanded if two 1300 and 1550 nm lasers were used. Unfortunately, germanium APD's required to detect the longer wavelength do not have the necessary gain nor SNR to resolve the strain produced by low amplitude SAW. We are thus forced to using 850 nm lasers due to the spectral limitation of the silicon APD. Although the two-wavelength stabilization technique does not totally eliminate the fading problem, it has indeed improved the stability by at least two orders of magnitude over that of a conventional single wavelength interferometer system. The stabilization has been achieved without the use of active feedback circuitry to compensate for phase drifts.

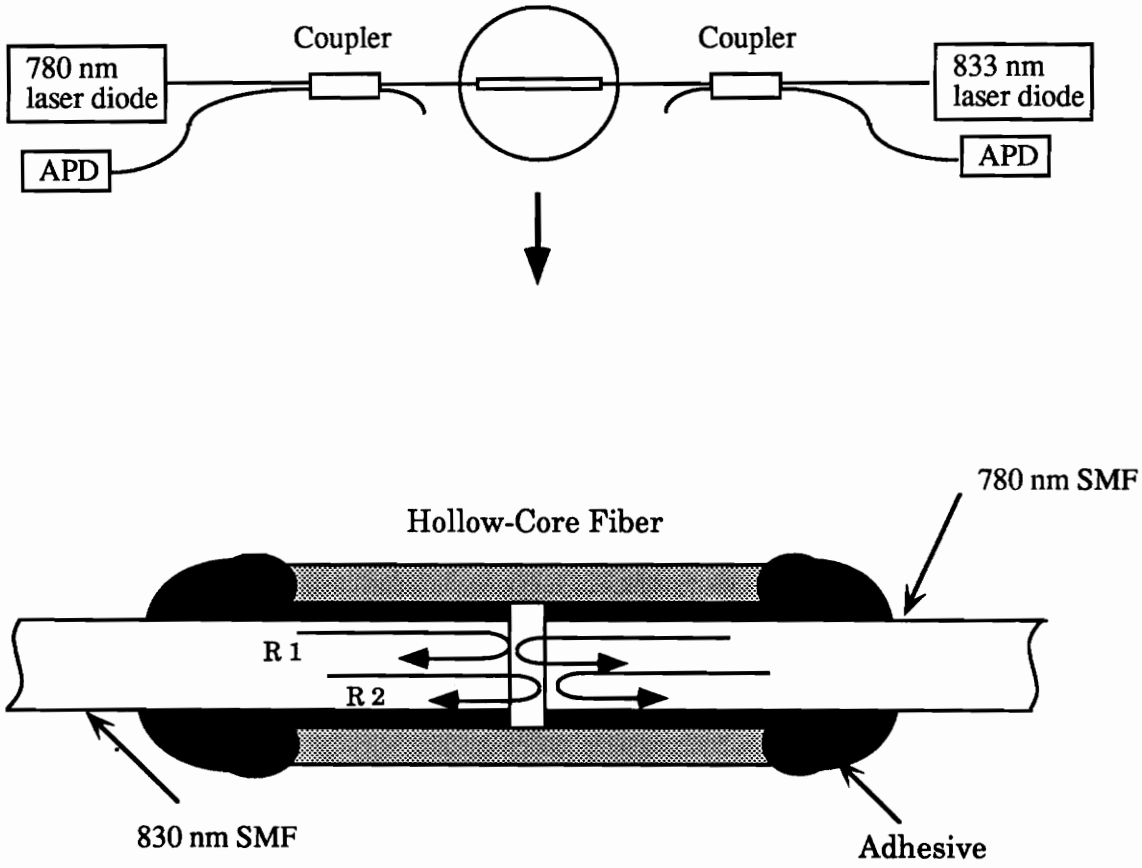

Figure 4.11 Setup for a stabilized phase sensor using a dual wavelength scheme.

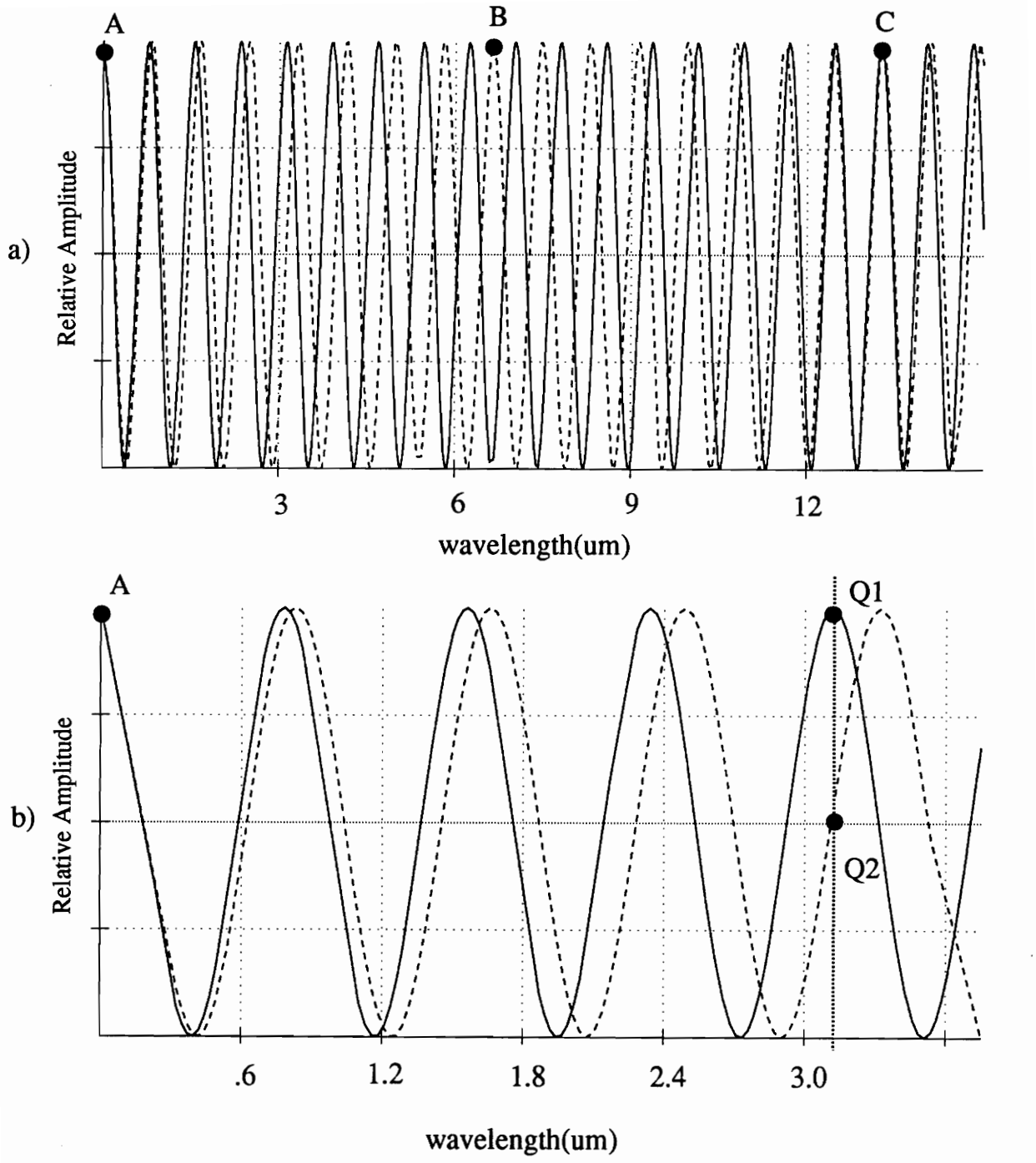

Figure 4.12 Beat frequency between two different wavelengths.

a) Dashed line represents 830 nm laser and solid line represents 780 nm laser.
b) Expanded view showing the 90^0 phase shift occuring between the two curves.

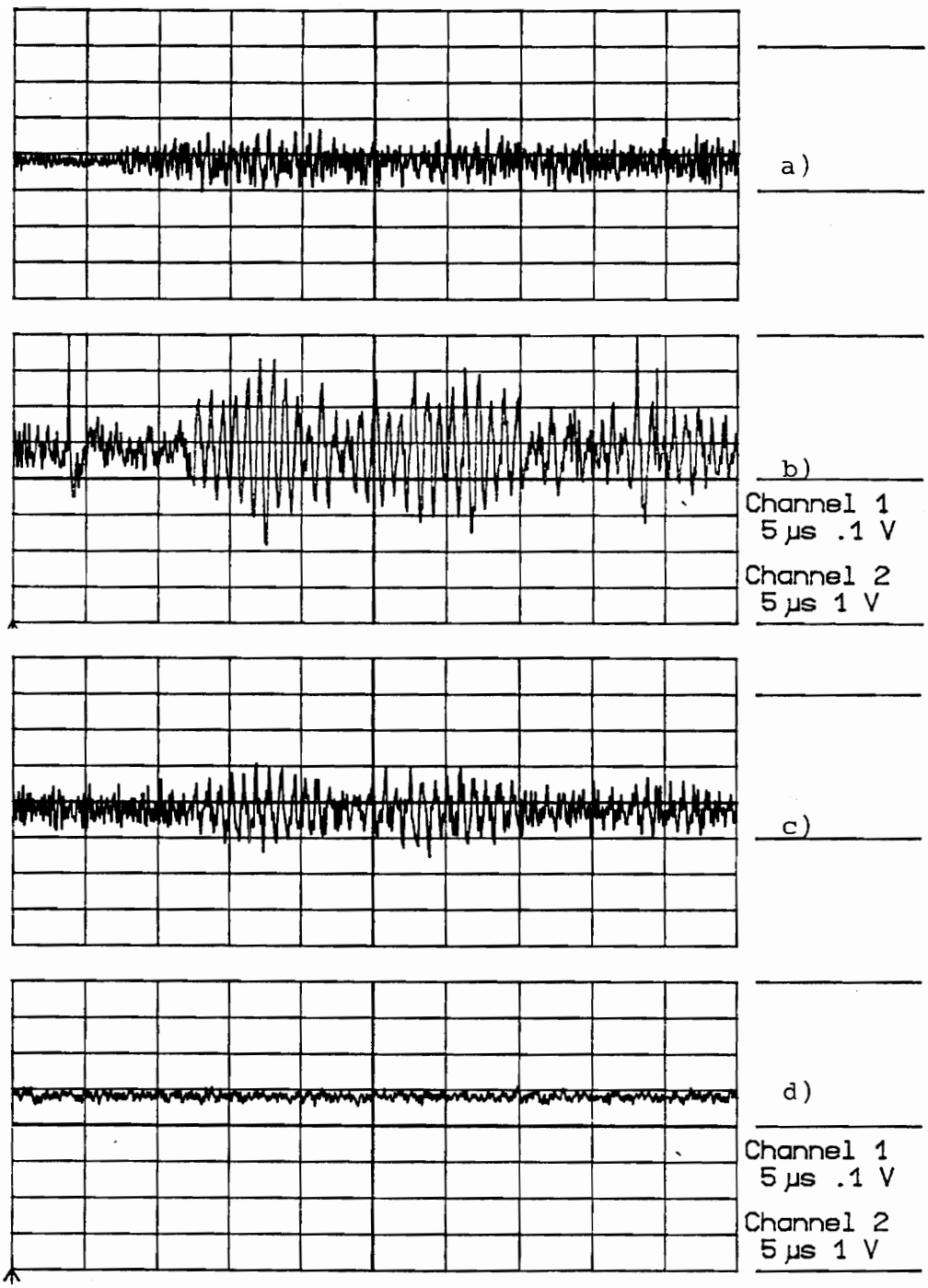

Figure 4.13 Stabilized output signals from an EFPI utilizing two wavelengths.

a) T=23 ^{0}C, λ_1=830 sensor is out of Q-point and b) T=23 ^{0}C, λ_2=780 sensor is at Q-point. c) T=30 ^{0}C, λ_1=830 sensor is at Q-point, and d) T=30 ^{0}C, λ_2=780 sensor is out of Q-point.

5.0 CLOSING REMARKS

A detailed explanation of an interferometric surface acoustic sensor employing an extrinsic Fabry-Perot interferometer has been presented, both from the theoretical and experimental viewpoints. Low frequency impact generated stress waves and high frequency continuous waves have been characterized with this sensor. It was shown that the sensor is a linear device provided that the amplitude of the signal is small, and that the sensor is operated at its quadrature point.

The stabilization of the sensor was also discussed and demonstrated because it is an important criterion for the continuous operation of the sensor. This is especially true if the sensor is exposed to temperature variations where the expansion of the silica fiber may in fact nullify the output of the sensor when the static phase difference cycles through the 180° angle. Using a dual-wavelength scheme, the problem associated with the interferometer fading has been minimized.

The EFPI system developed shows promise for the detection of SAW as well as the quantitative mapping of bulk stress wave fields in arbitrary material geometries. Due to the low-profile geometry of the sensor, such measurements may allow unique minimally intrusive opportunities to observe internal material characteristics.

APPENDIX A.1 BCD to ASCII conversion program

```
15   INPUT " Enter Input Filename   : ", FILNM$
17   INPUT " Enter Output Filename : ", OFILNM$
20   OPEN FILNM$ FOR INPUT AS #1
22   OPEN OFILNM$ FOR OUTPUT AS #2
25   ON ERROR GOTO 15
28   CLS
30   JJ = 0
35   GOSUB 600
40   INPUT #1,II%
50   IF 60 GOTO 40
70   INPUT #1,II%
71   IF (CHR$(II%) = 'A') GOTO 75
72   GOTO 40
75   JJ = JJ+1
80   IF JJ = 2 GOTO 140
90   GOTO 40
100  CLOSE #1
110  END
140  INPUT #1,II%
160  NBYT% = II%
170  INPUT #1,II%
190  NBYT% = NBYT% * 256 + II%
200  PRINT 'POINTS : ",NBYT%
205  PRINT
215  INPUT "Enter the SKIP Value : ", SKIP
220  FOR I = 1 TO NBYT%
230  INPUT #1,II%
260  IF INT(I/SKIP) = I/SKIP GOTO 265
262  GOTO 280
265  WRITE #2,II%
280  NEXT I
295  PRINT
300  INPUT " CONTINUE (Y) OR QUIT (N) : ", NXT$
310  CLOSE #1
315  IF (NXT$ = "Y" OR NXT$ = "y") GOTO 15
320  CLOSE #2
330  END
600  INPUT #1,II%
605  FILN$ = CHR$(II%)
610  INPUT #1,II%
620  IF (II$ = 0 ) GOTO 650
630  FILN$ = FILN$  + CHR$ (II%)
640  GOTO 610
650  PRINT "FILE : ", FILN$
660  RETURN
```

APPENDIX A.2 Spectral density calculation program

```
% This program is written for use with the Matlab software. It loads in
% the ASCII converted files from the oscilloscope and calls the [spdensit]
% subroutine to calculate the spectral density.

load i30.dat
[p_i30,fft_i30,i30] = spdensit(i30);
load i40.dat
[p_i40,fft_i40,i40] = spdensit(i40);
load i50.dat
[p_i50,fft_i50,i50] = spdensit(i50);
load i60.dat
[p_i60,fft_i60,i60] = spdensit(i60);
load i70.dat
[p_i70,fft_i70,i70] = spdensit(i70);
load i80.dat
[p_i80,fft_i80,i80] = spdensit(i80);
load i90.dat
[p_i90,fft_i90,i90] = spdensit(i90);

% This function calculates the spectral density of a waveform
% The program first truncates the waveform into 1000 significant data points
% and zero pad it with 500 data point. The zero padding increases the
% resolution for the FFT which is calculated next. The final step calculates
% the power contained between the normalized range of frequency.

function [p_sig,fft_sig,sig]=spdensit(sig)
sig = sig(5500:6500);                          % truncate waveform
sig = [sig' zeros(1:500)];                     % zero padding
fft_sig = abs(fft(sig));                       % calculate radix-2 FFT
fft_sig = fft_sig(1:length(fft_sig/2));        % extract the FFT
p_sig = sum(fft_sig(40:90));                   % summing the power
                                               % content betw/ 2 minima

plot(1:100,fft_i30(1:100))
```

APPENDIX A.3 Derivation of the response of the EFPI in Equation 3.2.1

$E_{1r}=E_0 r\, e^{j\omega t}$, $E_{2r}=E_0 t\, r'\, t'\, e^{j(\omega t - \phi)}$, $E_{3r}=E_0 t\, r'^3\, t'\, e^{j(\omega t - 2\phi)}$, ...

$E_{nr}=E_0 t\, r'^{(2n-3)}\, t'\, e^{j(\omega t - (n-1)\phi)}$

$$E_r = E_{1r} + E_{2r} + E_{3r} + \ldots + E_{nr}$$

$$= E_0 r\, e^{j\omega t} + E_0 t\, r'\, t'\, e^{j(\omega t - \phi)} + \ldots + E_0 t\, r'^{(2n-3)}\, t'\, e^{j(\omega t - (n-1)\phi)}$$

$$= E_0\, e^{j\omega t}\left[r + r'tt'\, e^{-j\phi}\left[1 + (r'^2\, e^{-j\phi}) + (r'^2\, e^{-j\phi})^2 \right] + \ldots (r'^2\, e^{-j\phi})^{n-2} \right]$$

assuming $r'^2\, e^{-j\phi} < 1$, $n \to \infty$

using Taylor's appr. $\sum_{n=1}^{\infty} = 1 + x + x^2 + \ldots + x^n = \frac{1}{1+x}$

$$= E_0\, e^{j\omega t}\left[r + \frac{r'tt'\, e^{-j\phi}}{1 + r'^2\, e^{-j\phi}} \right]$$

$tt' = 1 - r^2$ and $r = -r'$

$$E_r = E_0\, e^{j\omega t}\left[\frac{r(1- e^{-j\phi})}{1 + r'^2\, e^{-j\phi}} \right]$$

$$I_r = \frac{E_r E_r^*}{2}, \qquad R = \frac{I_r}{I_i} = \left[\frac{E_{0r}}{E_{0i}}\right]^2 = r^2$$

$$I_r = E_0{}^2\, r^2 \frac{(1- e^{-j\phi})(1- e^{+j\phi})}{2(1 + r'^2\, e^{-j\phi})(1 + r'^2\, e^{+j\phi})}$$

$$= \frac{I_i 2r^2(1-\cos\phi)}{(1 + r^4) - 2r^2\cos\phi}$$

$$\frac{I_r}{I_i} = \frac{2R(1-\cos\phi)}{1 + R^2 - 2R\cos\phi}$$

APPENDIX A.4 Frequency response simulation program

```
% SAW on aluminum Program


k1=0.942 ;
mu=2.6e11; l=mu;
rho=2.7;

d=.104125*10^(-6);
A=.009;
L=.018;
ls=.833*10^(-6);
n=1;
phi=4*pi*n*d/ls;
c2=sqrt(mu/rho);
c1=sqrt((l+2*mu)/rho);
f=1*10^6;


for i=1:600
t=0:.01:2;
t=t*10^(-4)/i;
f=f+1*10^(3);
w=2*pi*f;
k=w/(k1*c2);
s=sqrt(k^2-(w/c2)^2);
q=sqrt(k^2-(w/c1)^2);
I=cos(8*pi*A*k*L*(1-2*q*s)/(ls*(k^2+s^2))*...
  sin(k*d/2)*cos(w*t-k*d/2)+phi);
soln(i)=max(I);
freq(i)=f;
end;
plot(freq,soln);
```

BIBLIOGRAPHY

1. S. Kessler et. al., Instrumented Impact Testing of Plastics and Composite Materials", ASTM Special Technical Publication, Maryland, 1986.

2. H. N. G. Wadley, "Acoustic Emission: Nature's Ultrasound", Review of Progress in Quantitative Nondestructive Evaluation, Vol. 5A, Plenum Press, New York, 1985.

3. R. Williams, Acoustic Emission, Adam Hilger, Ltd., Bristol, England, 1980.

4. H. Kolsky, Stress Waves in Solids, Dover Publications, Inc., New York, 1963.

5. An Introduction to Piezoelectric Transducers, Valpey-Fisher Corporation, Massachussette, 1972.

6. A. Dandridge, A. B. Tveten and T. G. Giallorenzi, "Homodyne Demodulation Scheme for Fiber Optic Sensors Using Phase Generated Carrier", IEEE J. Quant. Electronics, Vol. QE-18, No. 10, pp. 1647-1653, 1982.

7. K. Krakenes and K. Blotekjaer, "Sagnac Interferometer for Underwater Sound Detection: Noise Properties", Optics Letter, Vol. 14, No. 20, pp. 1152-1154, 1989.

8. K. S. Chiang, H. L. Chan and J. L. Gardner, "Detection of High-Frequency Ultrasound with a Polarization-Maintaining Fiber", J. Lightwave Tech., Vol. 8, No. 8 pp. 1221-1227, 1990.

9. J. J. Alcoz, C. E. Lee and H. Taylor, "Embedded Fiber-Optic Fabry-Perot

Ultrasound Sensor", IEEE Trans. Ultra., Ferro. and Freq. Contl., Vol.37, No. 4, pp 302-305, 1990.

10. K. A. Murphy, M. F. Gunther, A. M. Vengsarkar and R. O. Claus, "Quadrature Phase-shifted Extrinsic Fabry-Perot Optical Fiber Sensor," Opt. Lett., Vol. 16, pp. 273-275, 1991.

11. J. S. Sirkis and H. W. Haslach, "Interferometric Strain Measurement by Arbitrarily Configured, Surface-Mounted, Optical Fibers", J. Lightwave Tech., Vol. 8, No. 10, pp. 1497-1503, 1990.

12. D. A. Jackson, R. Priest, A. Dandridge, and A. B. Tveten, "Elimination of Drift in a Single-Mode Optical Fiber Interferometer Using a Piezoelectrically Stretched Coiled Fiber", Appl. Optics, Vol. 19, No. 17, pp. 2926-2929, 1980.

13. R. J. Wasley, Stress Wave Propagation in Solids, Marcel Dekker, Inc., New York, 1973.

14. W. M. Ewing, W. Jardetzky, and F. Press, Elastic Waves in Layered Media, McGraw-Hill Book Co., Inc., New York, 1957.

15. R. V. Schmidt, "Acoustooptic Interactions Between Guided Optical Waves and Acoustic Surface Waves", IEEE Trans. Sonics and Ultrason., Vol. SU-23, No. 1, pp. 22-33, 1976.

16. I. A. Viktorov, "Investigation of Methods for Exciting Rayleigh Waves", Soviet Physics-Acoustic, Vol. 7, pp. 236-244, 1962.

17. M. Abramowitz and I. Stegum, "Handbook of Mathematical Functions", Washington, DC: Nat. Bur. Standards, 1972.

18. A. Dandridge, A. B. Tveten, "Phase Compensation in Interferometric Fiber-Optic Sensors", Optical Soc. Am., Vol. 7, No. 6, pp. 279-281, 1982.

Vita

Tuan Anh Tran was born in Can Tho, Vietnam on October 30, 1965. He received the Bachelor of Science Degree in Electrical Engineering from Virginia Tech in May 1988. Upon graduation, he started work in the Fiber and Electro-Optics group under the supervision of Dr. R. O. Claus. He graduated with an M.S. degree from Virginia Tech in May 1991.

Tuan anh Tran